Nanomaterials Science

Correlating Structural and Catalytic Properties in AuPd Nanorods

Author
Liselotte Olthof

Supervision
Jessi van der Hoeven
Giorgio Totarella
Prof. dr. Alfons van Blaaderen
Prof. dr. Petra de Jongh

March 15, 2019

Universiteit Utrecht

Inorganic Chemistry and Catalysis
Soft Condensed Matter and Biophysics
Debye Institute for Nanomaterials Science
Utrecht University

Abstract

For the selective hydrogenation of 1,3-butadiene, just as for countless of other reactions, a catalyst that minimizes the trade-off between a high activity and high selectivity is very desirable. For example, in this reaction Pd-based catalysts are very active, but they are especially at low levels of alkadienes not very selective. On the contrary, Au has a much higher selectivity, but it is less active than Pd. By combining these two metals in a bimetallic catalyst, promising catalysts can be made with high activity and selectivity. For these bimetallic catalysts the influence of the metal composition, size and shape of the nanoparticle (NP) has been investigated. However, the effect of metal distribution of the two metal phases on catalytic performance is less well understood.

A systematic study on the influence of this metal distribution is quite difficult, since a change in the metal distribution often also affects other parameters, such as the size and morphology of the particle. In this work we therefore made use of a well-defined model system, which consisted of colloidally synthesized single crystalline Au-Pd core-shell nanorods with a protective mesoporous silica shell (AuPd@mSiO$_2$ NRs). The metal composition and Pd shell-thickness was controlled in the colloidal synthesis. Subsequently, the metal distribution was gradually changed from core-shell to alloyed via thermal treatment. By making use of High-Angle Annular Dark-Field, Scanning Transmission Electron Microscopy with Energy Dispersive X-ray spectroscopy (HAAFD-STEM/EDX) on thermally treated rods we could precisely follow the metal redistribution from core-shell to an alloyed structure. Transmission Electron Microscopy (TEM) imaging and absorption optical spectroscopy showed that the shape of the silica coated particles remained constant, which indicated that only the metal distribution was changed.

The rods, gradually varying from core-shell to alloyed, were used in the selective hydrogenation of 1,3-butadiene to butene in the presence of excess propene. We found that core-shell rods outperformed their monometallic and alloyed counterparts; upon alloying AuPd@mSiO$_2$ NRs with 8 atom% Pd the Turn Over Frequency (TOF) reduced from 26 to 0.30 s^{-1}, while the selectivity remained high(>88%). The catalytic behaviour of the core-shell rods was further explored by tuning the shell thickness from 1 to 8 layers of Pd. At 2 atomic layers the highest TOF was reached, while further thickening of the shell reduced both the activity and selectivity.

Our work shows the significant importance of the metal distribution on catalytic performance, indicating that catalytic behaviour of bimetallic catalysts can be further improved by precisely controlling the metal distribution.

Contents

1
Introduction

Alkenes obtained from cracking of crude oil contain polyunsaturated impurities, such as diolefins and alkynes, which can poison the catalysts used for the polymerisation of these alkenes [1]. Impurities need to be reduced up to $10\,\text{ppm}$ to prevent this poisoning [1]. One technique to remove these polyunsatured impurities is selectively hydrogenating it to alkenes. Pd-based catalysts are widely used for this [2–7]. The problem with pure Pd catalysts is that it only remains selective as long as its active sites are covered with alkadienes. However when the alkadiene level is low, the selectivity drops significantly, meaning that the undesired conversion of alkenes to alkanes starts to occur.

To improve the selectivity, Pd can be doped with other metals. For example, in industry Pd is doped with Ag which greatly improves the selectivity [3]. Additives can also help reducing the formation of oligomer deposits which can deactivate the catalyst [8]. While Pd based catalysts are primarily being used in industry, early experiments with Au based catalysts showed it's potency for selective hydrogenation, even though it is much less active than Pd [9]. Later studies with Au nanoparticle (NP)s further proved that Au can hydrogenate 1,3-butadiene without forming butane [10], but can also be used to selectively hydrogenate acetylene [11], propyne [12] and many more [13]. The group of Catherine Louis also investigated Au NPs for selective hydrogenation of 1,3-butadiene, but in an excess of alkenes, to mimic conditions close to those of real purification [14]. This reaction was used as a model, since (partial) hydrogenation of 1,3-butadiene gives 4 products, so not only activity but also selectivity could be studied. An excess of propene was used in stead of butene since in this way product and reactant alkene could easily be distinguished. With
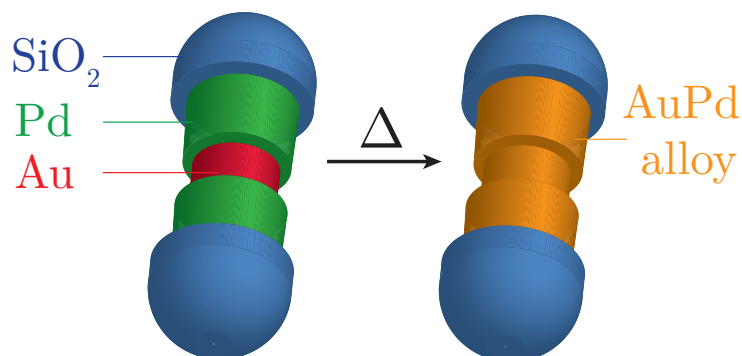
Figure 1.1: Graphical representation of SiO$_2$ coated Au-core Pd-shell NR and AuPd alloy NR.

this model reaction they found that 100% of butadiene was converted with only 100 ppm of alkane formation. To improve the activity of these Au catalysts in the same reaction, they used bimetallic AuPd catalysts [14, 15]. By tuning the Au/Pd ratio they combined the higher selectivity of Au with the activity of palladium.

The catalytic properties of bimetallic NPs can not only be tuned by varying the metal composition, but also by altering the distribution of the two metals within the particle. Hong *et al.* for example showed that the metal distribution in Au-Pd octahedral shaped nanocrystals largely influences the electrooxidation of formic acid [16]. The impact of the metal distribution was also indirectly shown by Masoud *et al.*, who used Au-Ag for selective hydrogenation of 1,3-butadiene and found that the catalyst lost half their activity, possibly due to Ag segregation to the NP surface [17]. This example emphasizes the need to take the atomic distribution into account when designing bimetallic catalysts.

Studying the effect of atomic arrangement in bimetallic particles on catalytic behaviour is however challenging, as it is difficult to controllably vary the metal distribution without changing other parameters in the system, such as the particle size and morphology. In this work we therefore used a well-defined model system, which consisted of colloidally synthesized single crystalline Au-core Pd-shell nanorod (NR) coated with a mesoporous silica shell. Within this system we controlled the distribution of the two metals via thermal treatment, as heating the core-shell rods induces the alloying process [18, 19]. See figure 1.1 for a graphical representation of a core-shell and alloyed AuPd@mSiO$_2$ NRs.

The metal distribution within the AuPd@mSiO$_2$ NRs was determined by mapping the location of Au and Pd with High-Angle Annular Dark-Field, Scanning Transmission Electron Microscopy with Energy Dispersive X-ray spectroscopy

(HAAFD-STEM/EDX). To check whether thermal treatment had influenced the shape of NRs, TEM images were made and absorption spectra recorded. For catalytic tests we used the same reaction as used in ref [14, 15, 17]; the selective hydrogenation of 1,3-butadiene in an excess of propene. As catalyst AuPd@mSiO$_2$ NRs, varying from core shell to completely alloyed and Au@mSiO$_2$ NRs were used. Furthermore, AuPd@mSiO$_2$ NRs with 1, 2, 5 and 8 atomic layers of Pd in its shell were tested to obtain more insight in how interaction between Au and Pd layers further affected the reaction.

2
Background

2.1 Au nanorod synthesis

The most common method in obtaining Au NRs is colloidal synthesis, where cetyltrimethylammonium bromide (CTAB) molecules in water are used as a shape directing surfactant [20]. This method is most popular due to the relative simple procedure, high NR yield and degree of particle size-control [21]. The seeded growth method allows the separation of two fundamentally different stages during rod synthesis: nucleation and growth. As for other colloidal NP syntheses, small and monodisperse nuclei are needed, which can only be made if the nucleation phase is very fast. To grow anisotropic shaped NPs you need kinetic control, since thermodynamic control would inevitably lead to an equilibrium shape, which cannot be achieved under the same reaction conditions as the nucleation phase. By separating the fast nucleation and slow growth phase from each other, rod shaped particles can be grown.

The current concept of the seeded growth method originates from the work of Jana *et al.* [22]. In their work the two steps were separated by using two different solutions: one for seed formation and one for rod growth. The seed solution was prepared by reducing Au(III) from $HAuCl_4$ to Au(0) with $NaBH_4$ in the presence of sodium citrate. These citrate capped seeds were added to a growth solution of $HAuCl_4$ as a gold source, CTAB as a template, ascorbic acid as reducing agent and $AgNO_3$ of which the role is discussed later. Nikoobakht and Al-Sayed later significantly improved this method with two modifications. First, they replaced the sodium citrate for CTAB which more strongly stabilized the seeds. Second,
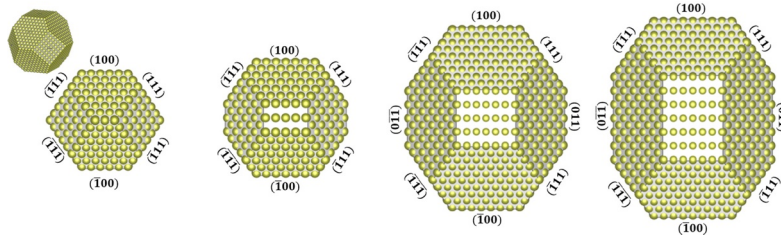
Figure 2.1: Gold nanocrystals during the symmetry breaking stage of NR growth, from ref [26]

they tuned the concentration of $AgNO_3$, by which they could control the aspect ratio [23]. This modifications significantly lowered the amount of spherical and other non-NR shaped particles that were formed.

The [$HAuCl_4$]:[$AgNO_3$] ratio not only determines the aspect ratio of the rods [23], as synthesis without $AgNO_3$ results in pentatwinned structured rods, in stead of single crystalline [24]. The responsible mechanism is however still subject to discussion. DFT simulations showed that a complex is formed between surfactant, bromine and silver that prevents growth of some facets [25]. Later Walsh *et al.* proposed a mechanism explaining the role of Ag in symmetry breaking [24, 26]. Their mechanism consists of several significant points. First, the crystal structure of the seed determines the final structure of the Au NR (single crystalline of pentatwinned). Second, Ag^+ stabilizes the formation of new {011} type facets, which eventually become the sides of the NR, see figure 2.1. Third, Ag atoms forming a layer on the sides of the rod are slowly replaced by Au atoms via galvanic replacement. After this new Ag^+ is deposited on the new Au surface. Due to this cycle, Ag never gets embedded inside the rod and growth can continue. Fourth, growth in the length direction of the rod happens due to Au deposition on unpassivated {111} surfaces at the tips of the rod. Finally, the rods 'mature', where initial lower-index facets are replaced with higher index facets, resulting in rounding of the rods. They therefore propose that the location of Ag in a mature rod is unlikely to represent the Ag location directly after rod formation. This corresponds to the findings of ref [27], who used EDX to show that Ag is present on all sides of Au NRs. This could however also indicate a different growth mechanism that does not rely on facet specific deposition of Ag.

The Au NR synthesis in this thesis was based on the procedure described by Murray *et al.* [28]. Murray *et al.* used a binary surfactant mixture of CTAB and sodium oleate (NaOL). With this method they could synthesize very monodisperse thin (diameter <25 nm) and thicker (diameter >30 nm) gold NRs. The NRs synthesized using this method are single crystalline, this in contrast to pentatwinned

structures that are formed when citrate capped seeds are used [21]. In this procedure a growth solution was made by dissolving $HAuCl_4$ in solution of $AgNO_3$ with a binary surfactant mixture of CTAB and NaOL. At the time of the original work of Jana *et al.* it was believed that CTAB acted as a micellar template, but in this method the CTAB concentration was below the critical micelle concentration ($0.037\,M < 0.9\,M$) [29]. Murphy *et al.* proposed that CTAB preferably binds to certain facets, such that the growth at the tips happens faster [30]. In this mechanism halide ions, among which Br^-, play an important role [31]. The other surfactant, NaOL, has a double bond which can slowly reduce Au(III) in $HAuCl_4$ to Au(I). Together they allow a slow, kinetically controlled, anisotropic growth. The seed solution consisted of a $HAuCl_4$ solution in CTAB, in which Au(III) is reduced to Au(0) by adding ice-cold $NaBH_4$. To the growth solution ascorbic acid was added, which, once the seed and growth solution have been mixed, results in the final reduction of Au(I) to Au(0).

2.2   Silica shell growth

In the next step of the synthesis procedure the Au NRs were coated with a mesoporous silica shell. This silica shell has several functions. Firstly, it acts as a stabilizer, enabling storage and further modifications while dispersed in other solvents than a CTAB in water solution. Secondly, the shell is known to help in maintaining the shape upon heating the rods [32]. Finally, the shell acts as a mould during the growth of a Pd shell [33]. NRs described in this thesis were silica coated by making use of the procedure of Gorelikov *et al.* [34]. A silica precursor, tetraethylorthosilicate (TEOS), was used for the coating. TEOS hydrolyses in the presence of water, enabling condensation into a gel, the former being a base or acid catalysed reaction [35]. In this case, NaOH was used to catalyse the reaction. Nooney *et al.* have proposed a mechanism for the formation of the silica shell [36]. After hydrolysis of TEOS, silica oligomers are formed. These oligomers form primary particles with CTAB in the reaction mixture. This is probably due to the interaction between positively charged ammonium head groups and negatively charged siloxide ions [37]. These CTAB/TEOS particles can aggregate to the CTAB molecules already attached to the surface of the gold NRs. The CTAB not only acts as an anchor point on which the silica can nucleate. Since the CTAB concentration of the reaction mixture ($1.5\,mM$), is far above the critical micelle concentration for CTAB in water of 0.9mM [29], micelles can be formed. These CTAB micelles on the gold surface act as a template for mesopores in the silica shell. After the growth of the silica shell is complete, the CTAB template needs to be removed, see
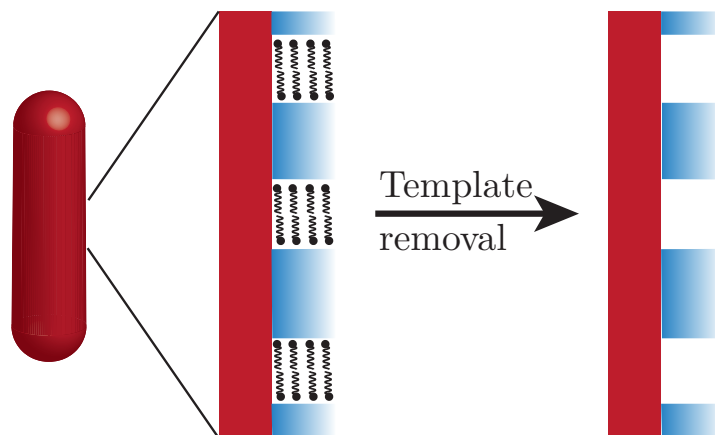
Figure 2.2: Graphical representation of cylindrical CTAB micelles which act as a template for mesopores in the silica shell on a Au nanorod surface. This micelles might be attached differently, since it is likely that a CTAB bilayer is present after synthesis.

figure 2.2. Typically organic ligands are removed by calcination, however under these conditions the NRs deform [33]. Therefore, in this work CTAB is removed by sonicating them in a $0.10\,\text{M}$ HCl in ethanol solution.

2.3 Palladium shell overgrowth

The next step of the synthesis is the deposition of a Pd-layer on the Au NRs to form a thin shell by making use of the procedure of Deng *et al.* [33]. The mesoporous character of the silica shell allows the particle to be overgrown from all directions. However, if the deposition happens too quickly, most of the Pd will nucleate outside the silica shell. Especially on a large scale, which is needed to obtain large quantities of material for catalysis, stirring is not fast enough to ensure proper mixing of the Pd precursor. The deposition reaction should thus proceed much slower. Therefore, the reaction speed was controlled by changing the pH, as showed by van der Hoeven *et al.* [19]. The Pd precursor, Na_2PdCl_4, was reduced with ascorbic acid. Ascorbic acid has three different forms which depend on the pH, see figure 2.3. Only the completely deprotonated form, ascorbate dianion, can reduce the Pd precursor. Due to the equilibrium, the ascorbate dianion gets replenished once it is consumed, keeping a low but stable concentration, enabling a slow deposition reaction.
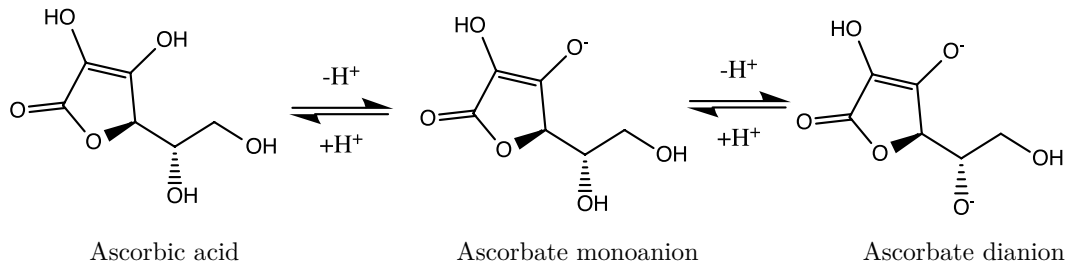
Figure 2.3: pH dependant forms of ascorbic acid

2.4 Etching of Au NRs

In previous work, before the second metal overgrowth, the Au NRs were always etched somewhat to make room for the second metal inside the silica shell [33]. For most of the Pd shell overgrowth syntheses, the SiO_2 shell accommodates enough space for the metal layer to be grown. It however appeared that approximately 22 atom% Pd was the physical maximum amount of Pd that fitted inside the SiO_2 shell. A small layer of Au was removed in order to make room for a thicker layer of Pd. This was done according to a method from ref[19]. This method is based on the procedure described by Deng *et al.* [33], but uses H_2O_2 as an oxidizing agent in stead of oxygen from the air.

2.5 Localized surface plasmon resonance

Surface plasmon resonance arises when electrons at the interface of a metal and a dielectric material, are stimulated by light. If such surface plasmon polaritons are confined in a metal particle which is smaller than the wavelength of the incoming light, the plasmon resonance is no longer delocalized. This leads to so called localized surface plasmon resonance (SPR). When the wavelength of light, thus the frequency of the photons, corresponds to the frequency of resonating electrons, a distinct maximum becomes visible at this wavelength in its optical absorption spectrum (λ_{max}).

Although the λ_{max} of gold nanospheres is quite insensitive to the diameter of the particle (core of 9 nm gives λ_{max}=517 nm and 49 nm λ_{max}=533 nm) [38], the SPR of Au NRs largely depends on the Aspect Ratio (AR) [28, 39, 40]. In anisotropic shaped particles, such as NRs two plasmon bands appear. This is due to light absorption and scattering along the long and short axis of the rod, causing the surface plasmon resonance to split intro transverse (TSPR) and longitudinal modes (LSPR). As the AR increases, the LSPR peak red-shifts, while the TSPR stays
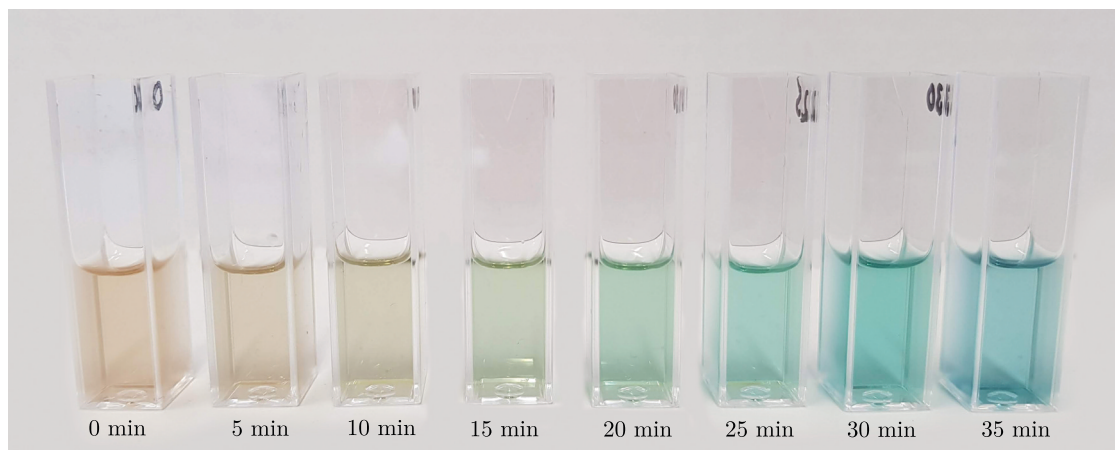
Figure 2.4: Colour change of Au@mSiO$_2$ NRs in methanol due to decreasing aspect ratio's (from left to right). On the left the original rods after SiO$_2$ coating, on the right after 35 min of etching. Au nanorods with L=69.7±6.0 nm, D=22.0±2.7 nm, V=24000±5600 nm^3.

relatively constant; for a Au NR with an AR between 2-5 the maxima vary from ∼700 to 900 nm [41]. This λ_{max} shift is shown in figure 2.4, where solutions of rods with decreasing ARs are shown. Next to this size dependant λ_{max}, larger NRs scatter light of almost an order of magnitude more efficient than small NRs (60 x 15 nm compared to 25 x 6 nm) [41, 42]. This strong plasmon resonance and great λ_{max} tunability makes them very useful materials for many applications, such as biosensors [40], cancer cell imaging and treatment [43], photocatalysis [44], data encryption [45] and many more.

2.6 Selective hydrogenation

The hydrogenation of 1,3-butadiene takes place according to the Horiuti-Polanyi mechanism and yields a mixture of three butenes, 1-butene, cis-butene and trans-butene and full hydrogenation leads to butane formation [46]. Traditionally it was believed that 1-butene is formed initially, which isomerises after readsorption. Later experiments with deuterium tracers and many types of supported metals, including Pd/Al$_2$O$_3$, proved a completely different mechanism [4]. As long as all active sites are occupied by 1,3-butadiene, the reaction takes place according to path A, see figure 2.5. However, once the 1,3-butadiene concentration drops and active sites become available, the initial products are readsorbed and the reaction proceeds according to path B. Now isomerisation and full hydrogenation competes and the product composition shifts to the thermodynamic equilibrium (trans-butene>cis-butene>1-butene). The adsorption strength of the reactants on the metal surface thus largely determines to what degree butane is formed [47].
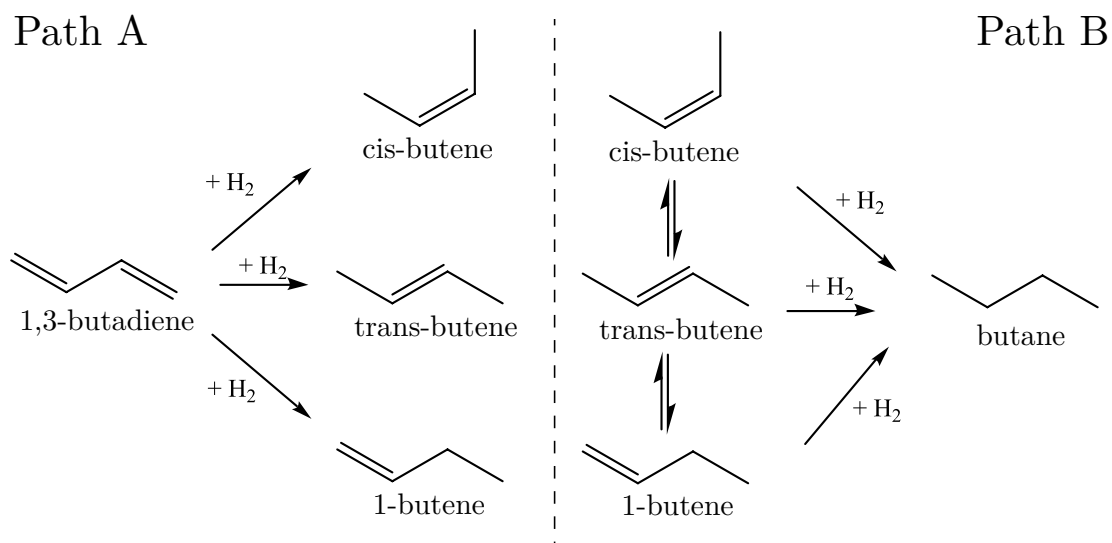
Path A   Path B

cis-butene   cis-butene

1,3-butadiene

trans-butene   trans-butene   butane

1-butene   1-butene

Figure 2.5: Two separate stages in butadiene hydrogenation. Pathways from [47]

When no readsorption takes place, the selectivity towards different butene isomers depends on which H_2-addition route is taken. 1,2-Addition leads to 1-butene formation, whilst 1,4 addition yields cis- and trans-butene [48]. Which product is formed preferentially is determined by formation of the respective transition states. There are several factors which influence the stability of these transition states. For example, in the 1,4-addition route a π-allylic bonded transition state is required, whilst this is not the case for 1,2-addition. As the d-band of a metal becomes more filled, the chances of forming a π-allylic transition state is reduced, thus increasing the rate of 1-butene formation[47]. This has been confirmed experimentally, showing that the yield of 1-butene increases with electronegativity of the metal [49]. Geometric effects can however also influence which transition states are more stable [50].

<div align="right">

3

</div>

Experimental

3.1 Materials

Aerosil (OX 50, Degussa), Ammonia (NH_3, $25\,wt\%$ in H_2O, Sigma-Aldrich), Ascorbic acid ($C_6H_8O_6$, 99%, Sigma-Aldrich), Cetyl trimethylammonium bromide (98%, TCI), Chloroauric acid ($HAuCl_4$, 99.9%, Sigma-Aldrich), Disodium tetrachloropalladate (Na_2PdCl_4, 98%, Sigma-Aldrich), Ethanol (99.5%, Sigma-Aldrich), Hydrochoric acid (HCl, $37\,wt\%$ in H_2O $12.2\,M$, Merck), Hydrogen peroxide (H_2O_2, $30\,wt\%$ in H_2O, Sigma-Aldrich), Silver nitrate ($AgNO_3$, 99.0%, Sigma-Aldrich), Sodium borohydride ($NaBH_4$, 98%, Sigma-Aldrich), Sodium hydroxide (NaOH, Merck, Emsure), Sodium oleate (NaOL, 97%, TCI), Tetraethyl orthosilicate (TEOS, 98%, Sigma-Aldrich), Toluene (Sigma-Aldrich), Propene gas (N2.5, Linde), 1,3-butadiene gas (N25, Air Liquide). All H_2O used during the synthesis was of miliQ grade ($18.2\,M\Omega\,cm$). All glassware used for synthesis was cleaned with aqua regia (HCl/HNO_3 in a 3:1 ratio by volume).

3.2 AuPd nanorod synthesis

The synthesis of mesoporous silica coated AuPd NRs was divided into several steps, which is graphically shown in figure 3.1. First, the Au rods itself were synthesized. Secondly, a silica shell was grown around the rods. After removal of the CTAB mesopore template, a Pd shell was grown on the Au rod inside the silica shell. Finally, the AuPd@mSiO_2 NRs were deposited onto a SiO_2 support.
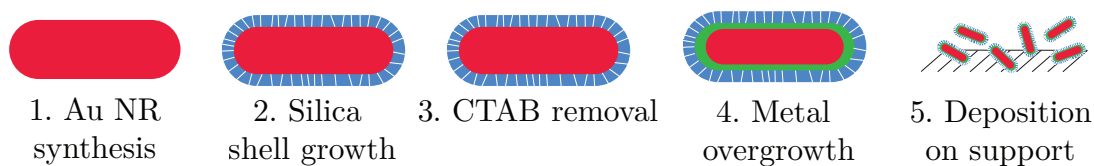
Figure 3.1: Schematic representation of the different synthesis steps of bimetallic AuPd NRs. Yellow: Au, green: SiO_2, red: Pd, white:mesopores

3.2.1 Au nanorod synthesis

The AuNRs were synthesized following a seed based method based on the work of Murray *et al.* [28].

Seed solution 10.0 mL of a 0.10 M CTAB solution was prepared in a 20 mL glass vial and heated in a 30 °C water bath while stirring at 400 rpm. Once the CTAB was dissolved, 51.0 µL of a 50.0 mM $HAuCl_4$ solution was added while still stirring. The seed solution turned orange immediately after adding the gold solution. 1.0 mL of an ice cold solution of 6.0 mM $NaBH_4$ was added to the seed solution while stirring vigorously (1000 rpm). After 2 min the stirring was stopped and the solution was let to age for 30 min. The solution turned light brown upon adding $NaBH_4$.

Growth solution An 500 mL Erlenmeyer flask, with 7.00 g of CTAB, 1.25 g NaOL and 250 mL H_2O was heated in a 50 °C water bath while stirring at 400 rpm for about 30 min. When the CTAB and NaOL were dissolved, the water bath was cooled down to 30 °C. 4.8 mL of 10.0 mM $AgNO_3$ (aq) was added to the growth solution while stirring. After 30 s 250 mL of 1.0 mM $HAuCl_4$ (aq) was added. The growth mixture was left to age for 90 minutes while stirring at 400 rpm. The mixture turned from orange to colourless, due to reduction of Au(III) to Au(I) by NaOL. Next 2.1 mL of HCl (12.2 M) was added and the mixture was stirred for 15 min and 1.25 mL 0.064 M ascorbic acid was added. Then, 0.80 mL of the seed solution was mixed with the growth mixture. After 1 min the stirring was stopped and it was left to grow overnight. Initially the mixture was colourless, but it slowly turned brown due to formation and growth of Au NRs. The synthesis mixture was centrifuged (45 min@9000 g) to separate the AuNRs from this mixture. Afterwards the NRs were washed with water by redispersing and centrifugation (45 min@8000 g). The particles were stored in 40.0 mL 5.0 mM CTAB to prevent aggregation.

3.2.2 CTAB coating

In a 300 mL Erlenmeyer flask, AuNR were diluted with water such that the absorption maximum of the LSPR peak was 10 (2.5× concentrated to initial synthesis mixture) and the total CTAB concentration was 1.5 mM. Therefore, 40 mL of Au NRs were added to 20 mL 5.0 mM CTAB water and 120 mL water. The flask with now in total 200 mL was placed in a 30 °C water bath, while stirring at 400 rpm with a large magnetic stirring bean. 2.0 mL of 0.10 M NaOH was added to this. After 5 min 0.60 mL of 0.90 M TEOS in ethanol (20 vol%) was slowly added, this was repeated twice with intervals of 45 min. The silica shell was let to grow for 24 h while stirring. The rods were separated from the reaction mixture by centrifugation (50 min@8000 g), redispersed in water, centrifuged (50 min@8000 g), redispersed in ethanol, centrifuged (60 min@6000 g) and redispersed in 30.0 mL ethanol.

To remove the CTAB template, the rods were first diluted with ethanol such that the absorption of the LSPR peak was 4. Concentrated HCl was added such that the HCl concentration in ethanol was 0.10 M. This mixture was sonicated for 30 min. To prevent etching, the rods were washed three times with ethanol by centrifugation (30 min@10.000 g) and redispersion. The rods were stored in 10.0 mL ethanol.

3.2.3 Etching

The Au core size was adjusted by oxidatively etching the rods inside the silica shell by making use of the procedure described in [19, 33]. To this end, 2.5 mL of Au@mSiO$_2$ NRs, were centrifuged 10 min@8500 g after which the ethanol was removed. The rods were subsequently redispersed in 50.0 mL methanol in a 100 mL Erlenmeyer (such that [Au NR] was 2.5× concentrated with respect initial synthesis), which was placed in a 60 °C water bath. After heating the mixture for 5 min, 1.0 mL HCl (12.2 M) and 1.0 mL H$_2$O$_2$ (0.20 wt%, 65 mM) was added while stirring at 400 rpm. After 20 min the reaction was stopped by quenching with about 50 mL cold methanol and simultaneously placing the Erlenmeyer in a cold water bath. The rods were separated from the etching mixture by centrifuging for 30 min@8500 g. After washing twice by centrifugation (20 min@8500 g) and redispersing in 20 mL ethanol, the rods were stored in 3.2 mL ethanol. The etched Au NRs are denoted as LO-015-E in this thesis.

Above mentioned method was also performed on a 10× smaller scale. At this scale a 0.50 mL sample was taken every 5 min, diluted 4× with ice-cold methanol, and an adsorption spectrum recorded, to determine how long the rods needed to be etched to get the desired Au core size.

Table 3.1: Used reaction parameters for AuPd NR synthesis with 2, 4, 8, 21 and 32 % Pd. AuNRs@SiO$_2$ originating from different batches were used (average AR=3.1), see 4.1. AA=ascorbic acid.

Sample	Au NRs		H$_2$O	HCl	Na$_2$PdCl$_4$		AA	
	Origin	mL	x (mL)	q (mL)	y$_1$ (mL)	y$_2$ (mM)	z$_1$ (mL)	z$_2$ (mM)
Pd A (2%)	LO-002	5.0	250	2.50	2.50	0.75	2.50	3.0
Pd B (4%)	LO-002	5.0	250	2.50	2.50	1.50	2.50	6.0
Pd C (8%)	LO-004	5.0	200	2.00	2.00	2.25	2.00	9.0
Pd D (21%)	LO-011	5.0	240	2.40	2.40	5.50	2.40	22.0
Pd E (32%)	LO-15-E	2.9	145	1.45	1.45	8.00	1.45	32.0

3.2.4 Ag removal

Ag present in the rods could influence the selectivity of the NRs. We therefore attempted to remove Ag from Au@mSiO$_2$ NRs, by washing them in a mixture of H$_2$O$_2$ and NH$_3$ in water. This etching solution was prepared by adding 175 µL NH$_3$ (25 wt%, 13.4 M) and 283 µL H$_2$O$_2$ (30 wt%, 9.8 M) to 4.54 mL H$_2$O.

1.35 mL of LO-015 Au NRs were centrifuged (15 min@10.000 g) and redispersed in 1.8 mL H$_2$O, such that the Au NR were 33 × concentrated compared to the initial synthesis. 200 µL of the etching solution was added, and the mixture was sonicated for 10 min. To remove the etching solution the rods were centrifuged (13 min@10.000 g), washed twice with 3 ml H$_2$O and once with 4 mL ethanol. Afterwards the rods were redispersed in 1.3 mL ethanol.

3.2.5 Pd shell growth

5.0 mL Au@mSiO$_2$ NRs were centrifuged (20 min@10.000 g), the supernatant removed and redispersed in x mL H$_2$O, such that the absorption maximum of the LSPR peak was 2. q mL of 0.1 M HCl and y$_1$ mL of y$_2$ mM Na$_2$PdCl$_4$ was added while stirring magnetically at high speed (800 rpm). Then z$_1$ mL of z$_2$ mM ascorbic acid in H$_2$O was added while still stirring, see table 3.1. The mixture turned from brown to green-black. The colour was darker with increasing Pd concentration. The mixture was let to react for 30 min while stirring at 400 rpm. The AuPd@mSiO$_2$ NRs were separated from the reaction mixture by centrifugation (30 min@4000 g). Next, the rods were redispersed in H$_2$O, centrifuged (30 min@4000 g), redispersed in ethanol, centrifuged (30 min@4000 g) and finally redispersed in 5.0 mL ethanol. The samples were stored in the fridge, to slow down oxidation of the rods.

3.2.6   Deposition

For the catalytic tests rods were deposited onto a fumed mesoporous silica support (Degussa Aerosil OX 50). The Brunauer–Emmett–Teller (BET) surface area of the used support is 35-65 $m^2 g^{-1}$ as reported by the manufacturer.

x mL of AuPd@mSiO$_2$ NRs NRs in ethanol were added to 1.0 g of SiO$_2$ support in a small vial, such that the total metal loading on the SiO$_2$ was 0.20 wt% and for Au@mSiO$_2$ NRs 1.0 wt%. This mixture was sonicated for about an hour, or until it became liquid like. About 14 mL of toluene was added and the vial was sonicated for a few minutes. After centrifugation (5 min@500 g) the colourless supernatant was removed, the powder dried under N$_2$-flow for a few minutes and further dried in an oven at 60 °C for the night. Once the sample was completely dry, indicated by the light blue colour of the powder, it was sieved (fraction 90-212 µm. The powders were stored in the dark to prevent oxidation of the rods by light. The supported NRs are indicated in this thesis as Au NRs@SiO$_2$ and AuPd NRs@SiO$_2$ for Au@mSiO$_2$ NRs and AuPd@mSiO$_2$ NRs respectively.

3.3   Ex-situ heating

The NRs were heated in three different ways. Firstly, deposited onto a TEM grid, heated in a tube oven. Secondly, while deposited onto SiO$_2$ support, heated in the catalytic set-up and finally, a dried droplet in a glas vial, heated in a tube oven.

On a TEM-grid

A droplet of AuPd@mSiO$_2$ NRs (8 atom% Pd) in ethanol, was dropped onto a TEM-grid. The TEM-grid was placed in a small glass vial and heated in a tube oven. While under a H$_2$-flow of around 100 mL min^{-1}, the oven was heated with 2 °C min^{-1} to 250, 300, 325, 350, 375, 400 and 450 °C and kept at that temperature for 1 h. As a means of reference Au@mSiO$_2$ NRs were heated in the same way to 250 °C, 350 °C and 450 °C.

On SiO$_2$ support

For each run 20 mg of AuPd NRs@SiO$_2$ (0.2 wt% with 8 atom% Pd) was placed inside a glass reactor. This reactor was heated in the oven with 2 °C min^{-1} to 250 °C, 300 °C, 325 °C, 350 °C, 375 °C, 400 °C and 450 °C and kept at that temperature for 1 h, while under a H$_2$-flow of 50 mL min^{-1}. After cooling down, a few mg of the support with rods was dispersed in ethanol by sonication. A droplet of the fluid was dropped onto a TEM grid.

The atomic distribution of NRs on the TEM grids from both methods (directly heated on the grid and on the support) was analysed by using HAAFD-STEM/EDX. An Energy Dispersive X-ray spectroscopy (EDX) element map of at least 4 NRs was made per heating temperature and method.

In a glass vial

50 µL of Au@mSiO$_2$ NRs or AuPd@mSiO$_2$ NRs (8 atom% Pd) in ethanol, was put in 1 mL glass vials. These vials were heated in a tube oven under a hydrogen flow of $\sim$100 mL min^{-1} to 250 °C, 450 °C and 650 °C. The rods were redispersed by sonicating and redispersing them in $\sim$2 mL ethanol.

3.4 In-situ heating

The in-situ heating experiment was done in a FEI Talos F200X operated at 200 kV with a heating holder from DENSsolutions. A mixture of AuPd NRs@SiO$_2$ with 6, 9, 21 and 43 atom% Pd was dropped onto a SiN$_x$ heating chip (Wildfire nanochip). The temperature of the heating chip was raised with 3 °C min^{-1}, and kept constant at 250, 300, 325, 350, 400, 450, 500, 550, 600, 650, 700 and 750 °C for 15 min. At each of these temperatures an EDX map with an acquisition time of 500 s was made and the probe current was 700 pA. To limit the exposure of the sample to the electron beam, the sample was only illuminated the EDX measurements.

3.5 Catalytic tests

For the selective hydrogenation of 1,3-butadiene a Pyrex glass plug-flow reactor with a diameter of 4 mm was used. The AuPd NRs@SiO$_2$, were first reduced *in situ* under pure H$_2$ (50 mL min^{-1}) from room temperature to different temperatures, depending on the desired degree of alloying, see table 3.2 (ramp 2 °C min^{-1}, hold 1 h at the desired temperature). All AuPd@SiO$_2$ samples contained 0.2 wt% metal and were, if necessary, diluted with Aerosil 50 (sieved 90-212 µm) to compensate for varying catalytic activity, see also table 3.2. For reference purposes, a run was performed with 4.86 wt% Pd NP@SiO$_2$ (average particle size 6.14 $\pm$2.54 nm, synthesized by Jessi in 12/2011, see figure 3.2). Au NRs@SiO$_2$ with 1 wt% loading was also tested.

After the *in-situ* reduction, the reactor was cooled down to 30 °C whilst still under H$_2$-flow. Then the reactor was exposed to a flow of 50 mL min^{-1} with 0.3 % 1,3-butadiene, 31 % propene, 20 % H$_2$ and helium as balance. The propene bottle also contained propane, resulting in 0.1 % propane in the flow. While
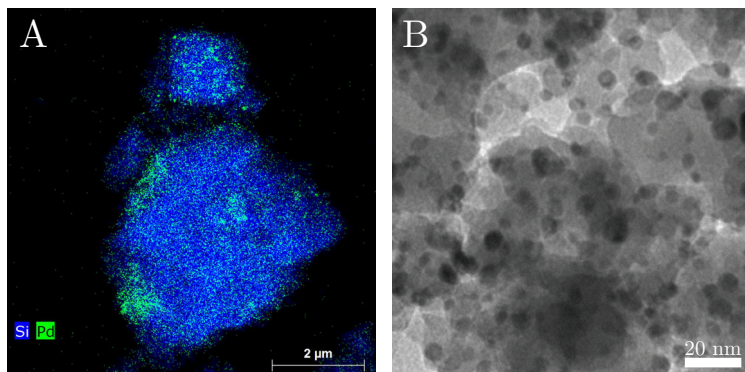
Figure 3.2: a) HAADF-STEM/EDX image of Pd@SiO$_2$ reference sample with 4.86 wt % Pd as determined by EDX. b) TEM image of Pd@SiO$_2$. Average particle size 6.14 ±2.54 nm. Synthesized by Jessi on 12/2011.

heating to 300 °C with a ramp of 1 °C min^{-1}, every 15 min (thus every 15 °C) a Gas chromatograph (GC) was recorded. For every experiment the initial gas concentrations were determined by recording two GC whilst the reaction gas was still running over the bypass.

3.6 Characterisation techniques and calculations

3.6.1 NR analysis

All samples for electron microscopy were prepared by drying a droplet of NRs in ethanol on a copper Transmission Electron Microscopy (TEM) grid (200 mesh, Formvar/carbon film). For supported NRs some of the SiO$_2$-support was sonicated in about 1 mL ethanol, after which a droplet was dried on the grid.

TEM Most Bright Field (BF) TEM images were made with a FEI Technai 10 operated at 100 kV. Some BF images were made with the FEI Talos F200X operated at 200 kV.

Particle dimensions Dimensions of rods were measured using ImageJ software from TEM-BF images. All given diameters (D) and lengths (L) were averaged over 50 particles. The volume and surface of the rods was approximated using:
$V_{rod} = \frac{1}{4}\pi D^2(L - \frac{1}{3}D)$ and $A_{rod} = \pi * L * D$.

Table 3.2: Overview of loaded catalyst per experiment. a) Experiments with AuPd NRs@SiO$_2$ with 8 atom% Pd, varying from core-shell to alloyed. b) Experiments with Au NRs@SiO$_2$ and AuPd NRs@SiO$_2$ with increasing Pd shell thickness. With structure of the particle, Pd content, the temperature used for the pretreatment, amount of loaded catalyst, weight loading and total metal content present in the reactor. The Pd content was determined with Inductively Coupled Plasma Atomic Emission Spectroscopy (ICP-AES). NP=nanoparticle and NR=nanorod

| Type	Pd content (%)	Pretreatment (°C)	Loading mg	Metal weight %	Total metal (μg)
a					
Core-shell	8	250	20	0.02	4
Core-shell	8	300	20	0.02	4
Core-shell	8	325	20	0.02	4
Partially alloyed	8	350	20	0.04	8
Partially alloyed	8	375	20	0.07	14
Alloyed	8	400	20	0.17	34
Alloyed	8	450	40	0.20	80
b					
Au NR	0	300	70	1	700
Core-shell	4	250	30	0.2	60
Core-shell	8	250	30	0.04	12
Core-shell	21	250	30	0.02	6
Core-shell	32	250	30	0.02	6
Pd NP	100	250	30	6×10^{-3}	2

Number of Pd layers The amount of atomic Pd layers for each of the different AuPd NRs was estimated with the following calculation. V_{pd} is the volume of one Pd atom determined from the van der Waals radius r_{Pd}=0.163 nm [51].

1. Surface to volume ratio: $\frac{A}{V} = \frac{A_{rod}}{A_{pd}} / \frac{V_{rod}}{V_{Pd}}$. Gives the fraction of Pd atoms at the surface, thus the fraction of Pd that the rods should contain assuming that all Pd is located at the surface.

2. For the next layer the L and D is recalculated: $D_{new} = D_{old} + 4 * r_{pd}$ and $L_{new} = L_{old} + 4 * r_{pd}$

3. The $\frac{A}{V} = $ ratio is recalculated and the result added to the previous fraction. This gives the fraction of Pd needed for 2 layers

4. Repeat step 2 and 3 until desired number of layers

HAADF-STEM/EDX All shown EDX maps were made with the FEI Talos F200X operated at 200 kV with a 700 pA probe current.

Table 3.3: Amount of Pd needed for 1-9 atomic Pd layers on a Au NR with D=21.8±2.1 nm and L=71.0±8.0 nm

Number of Pd layers	1	2	3	4	5	6	7	8	9
Pd needed (atom %)	4.5	8.8	13.0	17.1	21.1	25.0	28.9	32.6	36.25
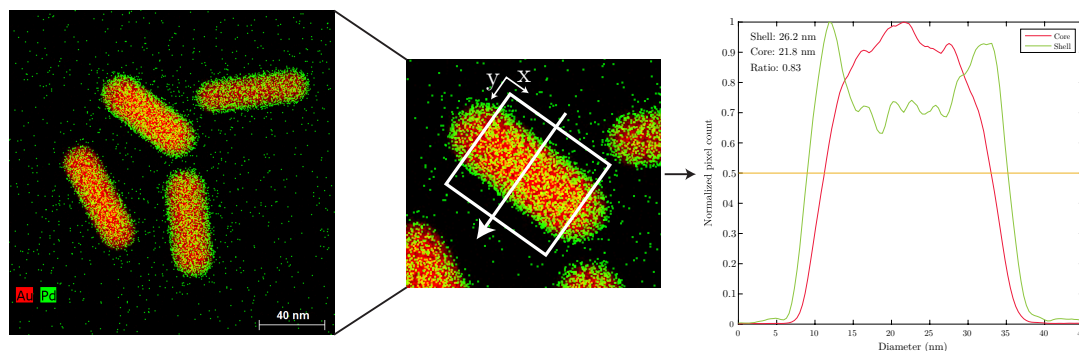
Figure 3.3: Graphical representation of quantification method of core and shell thickness from EDX maps. The EDX map corresponds to AuPd NRs with 8%Pd heated to 250 °C. Acquisition time=700 s.

Au Core and Pd shell mapping   The diameter of Au cores and Pd shells was determined from the EDX maps by making RGB-plots (red, green, blue) with a plug-in for ImageJ. In such a RGB-plot the amount of red and green pixels in the y-direction (diameter of the rod) were counted and averaged over the x-direction (length of the rod). The result was smoothed, normalized from zero to one and plotted. The data smoothing was performed with Matlab, using a moving average smoothing function with a bin size of 5 pixels. The thickness of the core and the shell was determined at the full width half maximum (FWHM) of the plot of the red and green pixel counts respectively, resulting in a core and shell thickness and thus a core-to-shell ratio. This method is depicted graphically in figure 3.3. The core and shell diameter and core-to-shell ratio after synthesis was averaged over 10 particles. For the alloying experiments the core-to-shell ratio was averaged over 4 particles.

Absorption spectroscopy   The absorption spectrum of dispersions of NRs were recorded with a Bruker Vertex 70 Fourrier Transform Infrared Spectroscopy (FTIR) with a quartz beamsplitter between 450-1200 nm, with averaging over 60 measurements.

ICP-AES   The Au, Pd and Ag metal content in finished Au@mSiO$_2$ NRs and AuPd@mSiO$_2$ NRs was determined with ICP-AES. For this 10 µL of NR sampe was added to 490 µL aqua regia (HCl/HNO$_3$ in a 3:1 ratio by volume). After 1 h

it was diluted with $4.5\,\mathrm{mL}$ H_2O and centrifuged for $5\,\mathrm{min@15.000\,g}$. The top $4.9\,\mathrm{mL}$ fraction was used for ICP analysis.

The analysis was performed with a PerkinElmer Optical emission Spectrometer Optima 8300 with a PerkinElmer S10 Autosampler. Gas flows of 8.0, 0.20 and $0.65\,\mathrm{L\,min^{-1}}$ were used for the plasma, auxiliary gas and nebuliser, respectively. The radio frequency power was set at 1500 W and the pump flow rate at $1.5\,\mathrm{mL\,min^{-1}}$.

3.6.2   Catalytic tests

For the catalytic tests a set-up in which a glass plug-flow reactor can be heated was used. Through this reactor different pretreatment gasses (H_2, N_2, air) and the reaction gas (H_2, 1,3-butadiene, propene and helium) can be flowed). For all tests a flow of $50\,\mathrm{mL\,min^{-1}}$ with $0.3\,\%$ 1,3-butadiene, $31\,\%$ propene, $20\,\%$ H_2 and helium as balance was used. The propene bottle also contained propane, resulting in $0.1\,\%$ propane in the flow. The reaction products were analysed with a GC coupled to a flame ionisation detector ().

Activity   From the reactant and product concentrations obtained from the GC, the conversion, TOF and H_2-selectivity was determined. The conversion was defined as the percentage of 1,3-butadiene molecules which were converted. From this the TOF (Turn over frequency), defined as the butadiene conversion per second metal per surface atom, was calculated. The amount of surface atoms was estimated as following:

1. Mass of a rod: $m_{rod} = \frac{V_{rod}}{\rho_{av}}$ with $\rho_{av} = x_{Au}\rho_{Au} + x_{Pd}\rho_{Pd}$. x_{Au} and x_{Pd} the atomic fractions as obtained from ICP and ρ_{Au} and ρ_{Pd} for fcc structured Au and Pd

2. Total surface area: $A_{total} = \frac{loadedmetal(g)}{m_{rod}} * A_{rod}$

3. Number of surface atoms: $\#_{atoms} = \frac{A_{total}}{A_{pd}}$ with A_{pd} the surface area of a Pd atom determined from the van der Waals radius

Selectivity   The selectivity is given as the H_2-selectivity, which shows the fraction of H_2 that was used for desired products (1-butene, cis-butene and trans-butene) compared to all used H_2.

4

Results and discussion

4.1 Characteristics of Au NRs

4.1.1 NR dimensions

The Au NR synthesis was performed four times. Optical absorption spectra were taken of all batches after SiO_2 coating, see figure 4.1. The LSPR peak of the batches was located at a very comparable wavelength, indicating that the rods from all batches had a similar particle AR. This was checked by determining the particle sizes from TEM images, see figure 4.2. Table 4.1 with the average length and width of the particles of the different batches indeed confirms that they were all very similar. The rods had a low monodispersity and no other Au particle shapes such as spheres, cubes or triangles were found. From LO-004 no dimensions were determined, but they should be similar to those of LO-002, considering the fact that the batches had a similar LSPR peak position. The thickness of the SiO_2 shell was determined from TEM and was on average 17.2±0.7 nm.

4.1.2 Attempted Ag removal

$AgNO_3$ was used during the synthesis to aid the formation of the NRs. As mentioned earlier, Ag can influence the selectivity of a Pd based catalyst. The final rods contained about 1.4 atom% Ag, as determined from ICP-AES. Therefore we attempted to remove Ag by washing Au@mSiO$_2$ NRs in a NH_3 and H_2O_2 solution. Afterwards an absorption spectrum was recorded to determine if the AR of the rods had changed, see figure 4.3. The LSPR peak shifted from 740 nm to 717 nm,
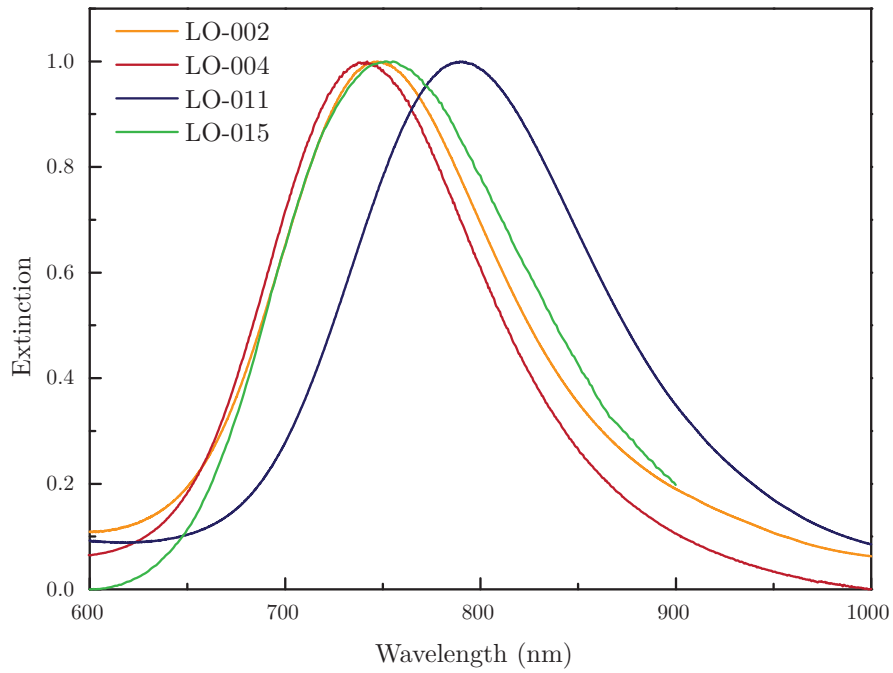
Figure 4.1: Normalized optical absorption spectra after synthesis of the Au NRs. The different spectra represent four separate batches, see table 4.1. The LSPR maxium were at 742 nm, 747 nm, 752 nm or 794 nm.
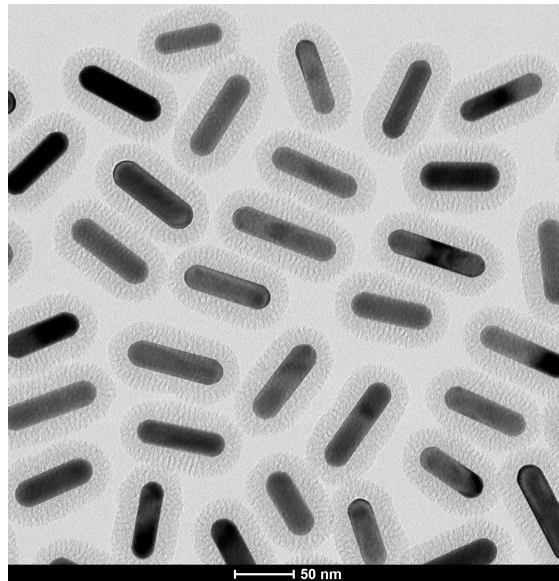

Figure 4.2: Bright field TEM image of LO-002 Au@mSiO$_2$ NRs with D=20.9±2.1 and L=68.7±6.0

Table 4.1: Dimensions of AuNRs from different syntheses batches and LO-015 after etching (see 4.2). Average length, width, aspect ratio, volume and surface area are shown.

Sample	Width (nm)	Length (nm)	Aspect ratio	Surface (nm^2)	Volume (nm^3)
LO-002	20.9±2.1	68.6±6.0	3.3±0.4	20800±5100	4420±700
LO-011	18.9±2.1	57.9±6.9	3.1±0.5	14600±3400	3440±550
LO-015	22.0 ±2.7	69.7±6.1	3.2 ±0.5	24100±5600	4830±680
LO-015-E	22.3 ±2.3	61.0±7.9	2.7±0.46	21200±5800	4280±800
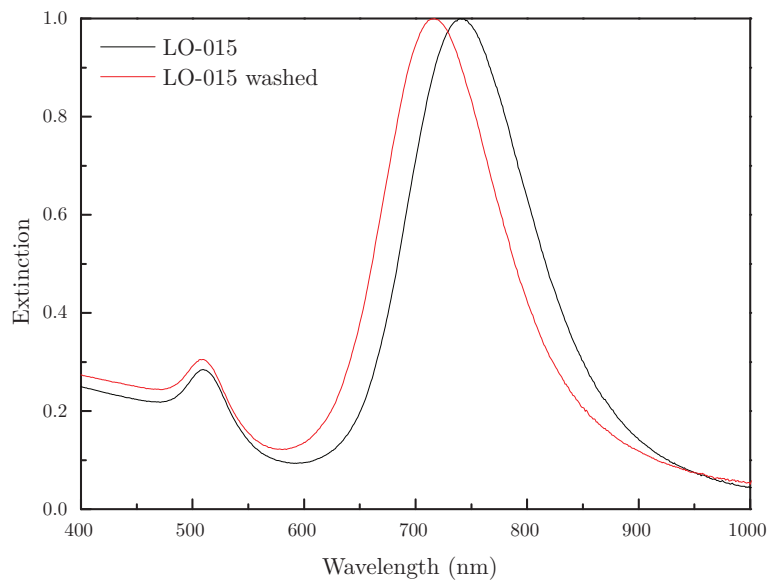
Figure 4.3: Extinction spectrum before and after washing with H_2O_2 and NH_3 of LO-015 Au@mSiO$_2$ NRs in ethanol with original Au-core size of L=69.7±6.1 nm, D=22.0±2.7 nm and V=24100±5600 nm^3.

indicating that the rods were etched somewhat by the treatment. ICP-AES showed that the treated rods contained about 1.6 atom% Ag, so the treatment did not remove any Ag. This washing solution is known to remove Ag from other metals [52], so possibly the Ag concentration was too low for this procedure to work.

4.2 Etching of Au NRs

To determine how long the rods had to be etched in order to free up enough space to grow a thick Pd layer but not remove too much of the Au core, the etching was first performed on a small amount of Au@mSiO$_2$ NRs. During this etching FTIR spectra were recorded. In figure 4.4 the spectra corresponding to 0-30 min of etching with intervals of 5 min are shown. For every 5 min the LSPR peak shifts
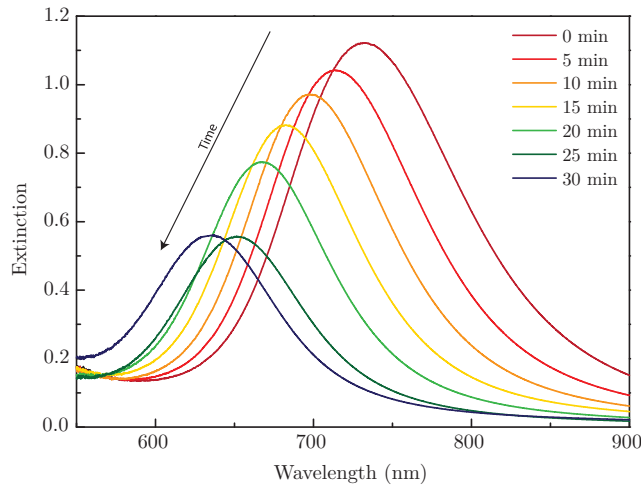
Figure 4.4: Absorption spectra of Au nanorods diluted 4x in methanol after 5, 10, 15, 20, 25, 30 minutes of etching in HCl and H_2O_2. Original Au core with L=69.7$\pm$6.1 nm, D=22.0$\pm$2.7 nm and V=24100$\pm$5600 nm^3.

about 15 nm and its intensity decreases. The intensity dropped due to a decrease of NR volume. The intensity of the peak corresponding to 25 min of etching was not representative as the sample was diluted more by mistake. As mentioned in chapter 2, the LSPR peak position of Au NRs depends on the AR and a lower AR results in a blue shift. The observed blue shift was thus caused by a decrease in AR of Au@mSiO$_2$ NRs due to preferential etching at the tips of the rods. This blue shift due to preferential etching was also shown by ref [33]. TEM images were also made of the rods before, after 30 min and 60 min of etching, see figure 4.5. These images show that the rods clearly became shorter but the SiO$_2$-shell shape remains intact, leaving some space between the rod and its shell.

From these experiments it was estimated that when stopping the etching at 20 min, only a small amount of Au was removed. Therefore, the experiment was repeated at a larger scale (2.5 mL Au@mSiO$_2$ NRs after silica coating in 50 mL methanol, 2.5$\times$ concentrated with respect initial synthesis). Herein, a batch of Au@mSiO$_2$ NRs was etched for 20 min. This changed the Au core from L=69.7$\pm$6.1 nm and D=22.0$\pm$2.7 nm to L= 61.02 $\pm$7.92 nm and D=22.26 $\pm$2.3 nm. The LSPR peak position changed from 752 to 667 nm, confirming that the etching mainly occurred at the tips.

4.3 Characteristics of AuPd NRs

After growing the Pd metal shell, the Pd content in AuPd@mSiO$_2$ NRs from different synthesis batches was determined with ICP-AES and was 2.51, 4.20, 8.30, 22.1 and 32.0 atom%.
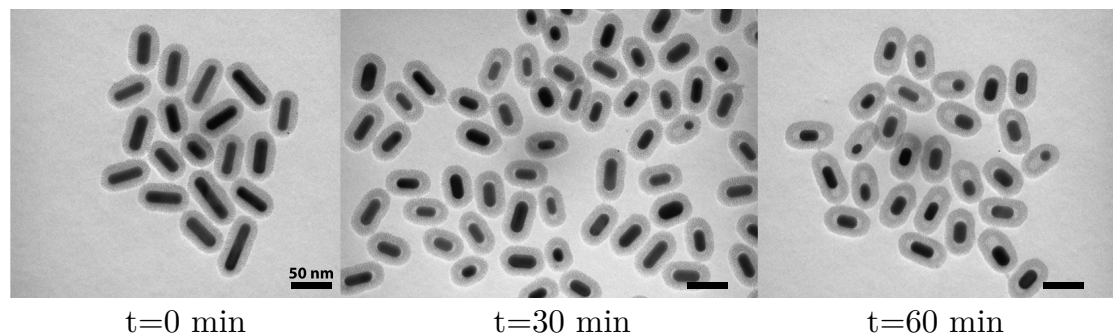
<div align="center">t=0 min   t=30 min   t=60 min</div>

Figure 4.5: TEM-BF images of Au nanorods after 0, 30 and 60 minutes of etching in HCl and H_2O_2. Au nanorods with original dimensions of L=69.7±6.1 nm, D=22.0±2.7 nm and V=24100±5600 nm^3

.

The rods were also characterised by HAADF-STEM/EDX. In figure 4.7 an overview of HAADF-STEM and EDX maps of corresponding batches is shown. The Pd content was also determined from these EDX maps, giving 5.0, 7.1, 13, 25 and 38 atom% Pd. For Au@mSiO$_2$ NRs the by EDX determined Pd content was 2.29 atom%, while ICP did not find any Pd. This showed that EDX erroneously counts other atoms as Pd atoms, explaining the higher values obtained with EDX. In figure 4.7 the Pd content in the rods as determined by ICP and EDX was plotted as a function of the Pd precursor concentration. The graph shows a linear relationship between the Pd precursor concentration present in the reaction mixture and final Pd content in the rods. This synthesis method thus allowed precise tuning of the thickness of the Pd shell on the Au@mSiO$_2$ NRs by varying the amount of Pd-salt.

The Pd shell thickness was measured from the EDX maps with RGB-profile plots. Such a profile plot was made for 10 particles per synthesis. The resulting averaged core- and shell thickness with corresponding core-to-shell ratio are given in table 4.2. As expected, the core-to-shell ratio decreases as the amount of Pd increases, with exception of the rods with 32.0 atom% Pd. The Au cores for this overgrowth were etched first, which mainly occured at the tips, lowering the initial AR. Note that AuPd@mSiO$_2$ NRs originated from different Au-core syntheses which had small AR variations.

4.4 Heating experiments

In order to precisely map the atomic distribution of the two metal phases upon heating, while making sure that the AR remained stable, several experiments were done, see figure 4.8. The rods were heated in three different ways: 1) deposited
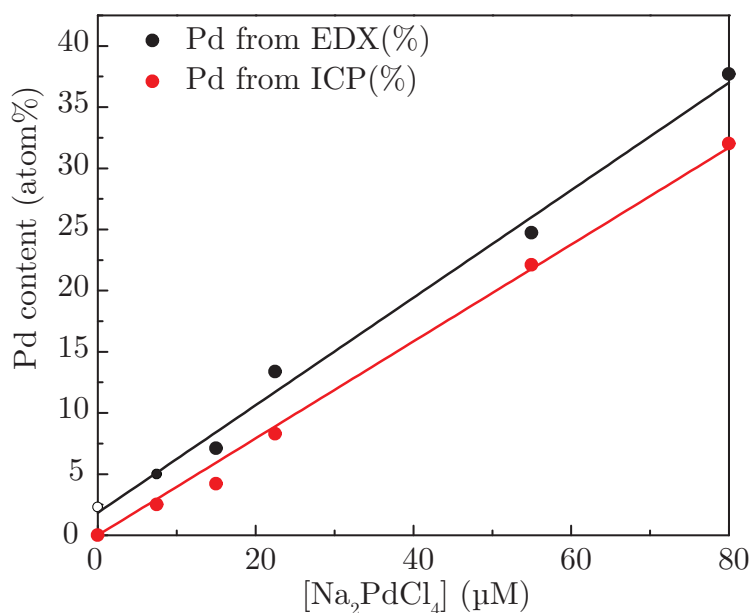
Figure 4.6: Atomic Pd percentages in AuPd@mSiO$_2$ NRs as determined from EDX and ICP-AES as a function of Na$_2$PdCl$_4$ concentration in the reaction mixture.

Table 4.2: Pd content per sample from ICP. Core- and shell thickness and core-to-shell ratio of different AuPd@mSiO$_2$ NRs syntheses as determined from EDX maps. Particle volume and surface area determined from TEM images

Sample	Pd atom %	Core (nm)	Shell (nm)	Core/shell ratio	Surface (nm^2)	Volume (nm^3)
Pd X	2.5	16.4±1.3	17.6±1.4	0.93±0.05	4060±680	17900±4700
Pd A	4.2	17.8±2.3	19.8±2.3	0.90±0.04	4860±750	23900±5300
Pd B	8.3	17.9±2.4	21.9±2.6	0.82±0.03	3560±650	21500±6400
Pd C	21	13.2±1.4	18.8±1.9	0.70±0.02	3670±590	15000±3800
Pd D	32	21.2±3.5	27.6±3.0	0.76±0.05	5470±1200	29900±9800

onto a TEM grid, heated in a tube oven, 2) a dried droplet in a glas vial, heated in a tube oven and 3) while deposited onto SiO$_2$ support, heated in the catalytic set-up. The rods obtained from these different heating treatments were analysed by TEM-imaging, EDX mapping and FT-IR absorption spectroscopy. This section discusses deformation and alloying behaviour of the NRs.

4.4.1 Deformation

From TEM-images of AuPd@mSiO$_2$ NRs with 8 atom% Pd and Au@mSiO$_2$ NRs (obtained from 1. rods heated on TEM-grid) the AR of 50 particles per heating temperature was determined, see figure 4.9. This figure shows that all rods, with
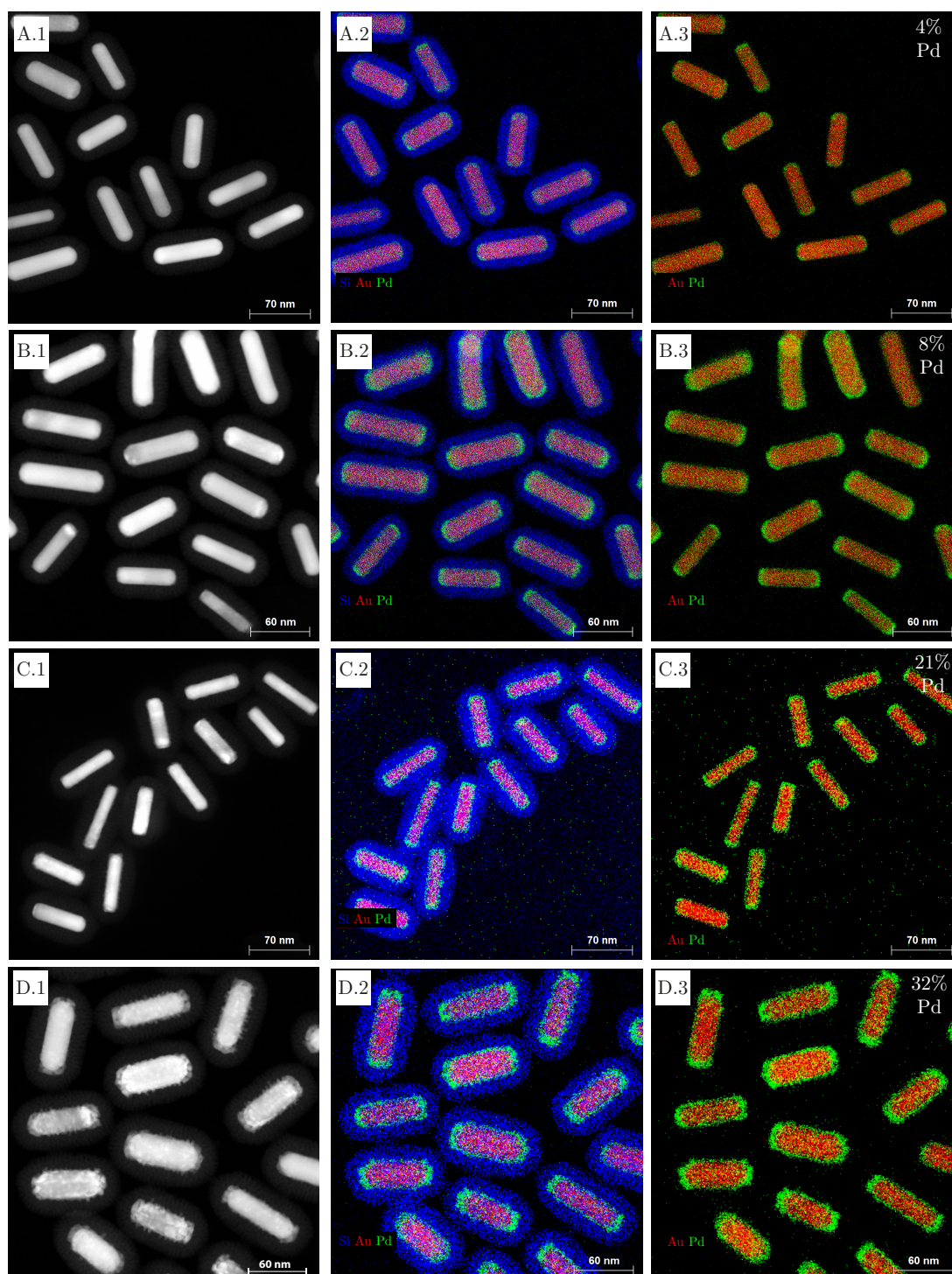
Figure 4.7: Overview of the AuPd NR from different syntheses. In the first column HAADF-STEM images, the second EDX maps with silica shell and the third EDX maps without the silica shell. Red pixels represent Au, green for Pd and blue for silica. The rows A-D correspond to the AuPd@mSiO$_2$ NRs with different palladium content of 4, 8, 21 and 32 atom% Pd, as shown in white on the last column.
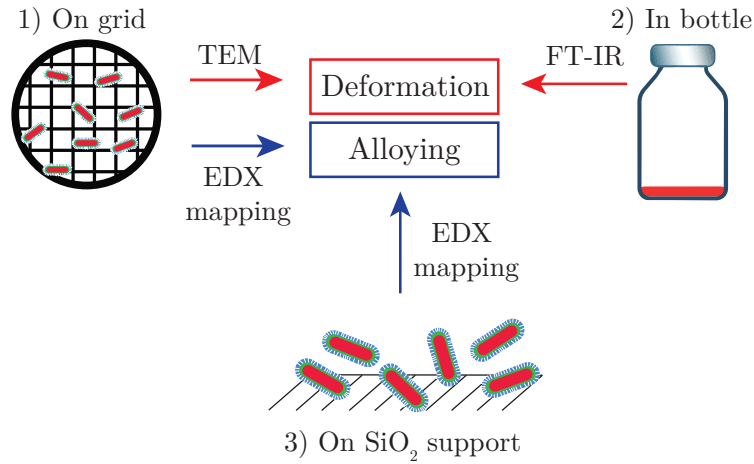
Figure 4.8: Graphical representation of different experiments performed to analyse the alloying and deformation of Au@mSiO$_2$ NRs, AuPd@mSiO$_2$ NRs and AuPd NRs@SiO$_2$.

and without Pd, do not deform significantly till 450 °C. Once heated to 650 °C the rods started to deform somewhat, and the AuPd@mSiO$_2$ NRs were slightly more stable than Au@mSiO$_2$ NRs. The extinction spectra confirmed this behaviour. In figure 4.10a and 4.10b respectively the extinction spectra of Au@mSiO$_2$ NRs and AuPd@mSiO$_2$ NRs (8 atom% Pd) which were heated to 250, 450 and 650 °C (2. in a glass vial) are shown. The LSPR peak λ_{max} of Au@mSiO$_2$ NRs after heating to 450 °C shifted slightly, however when heated to 650 °C a more significant blue shift appeared. The LSPR peak shift of AuPd@mSiO$_2$ NRs heated to 650 °C confirms that they indeed deformed slightly.

4.4.2 Alloying

The EDX maps corresponding to AuPd@mSiO$_2$ NRs (8 atom% Pd) heated on a TEM grid to 250, 300, 350, 400 and 450 °C are shown in figure 4.11. With increasing heating temperature the rods started to alloy more. To quantify how much the atomic distribution of the rods had changed, RGB profile plots were made to determine the core and shell diameter for 4 rods per heating temperature. From the core-to-shell ratio's the degree of alloying was calculated. This was defined as a scale from zero to one, with zero corresponding to the original core-shell ratio and one to a fully alloyed rod, where the core and shell are no longer distinguishable. The degree of alloying as a function of heating temperature can be found in figure 4.12a. Upon heating, the rods gradually transformed from core-shell to fully alloyed. The alloying temperature, which was defined as temperature at which the degree of alloying was 0.5, was 383 °C
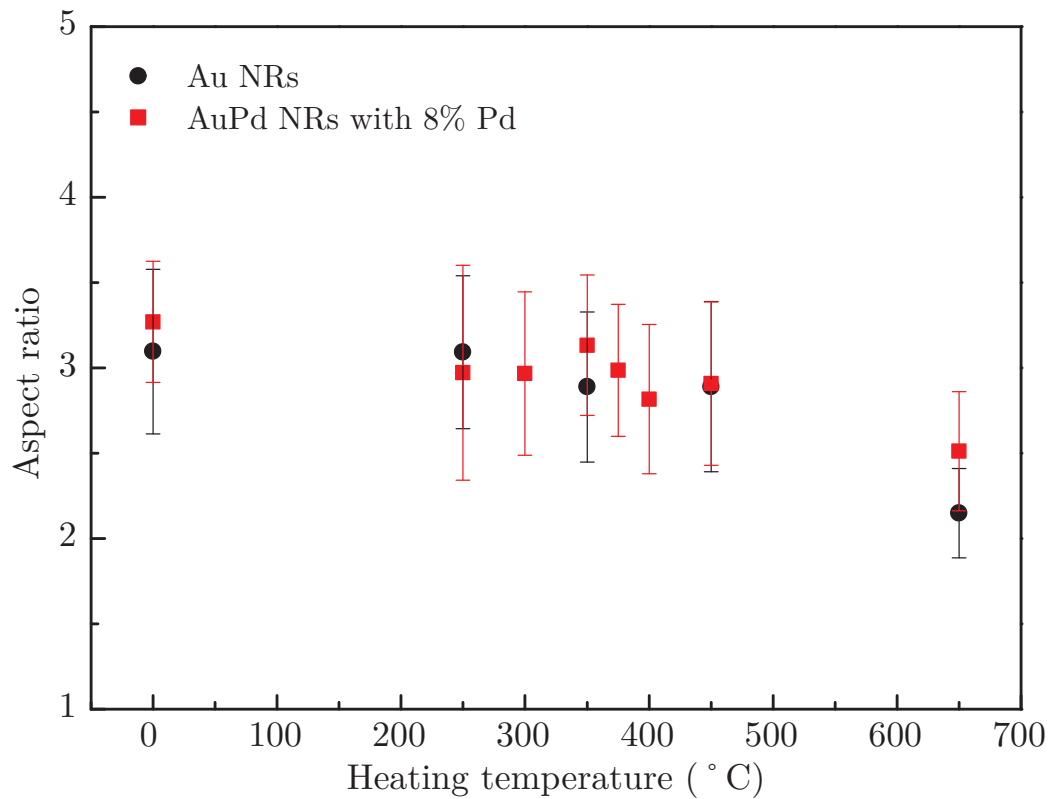
Figure 4.9: Aspect ratio of AuPd@mSiO$_2$ NRs (8 atom% Pd) and Au@mSiO$_2$ NRs after heating to different temperatures. Deposited onto a TEM-grid and heated in a tube oven under H$_2$-flow with $2\,^\circ\mathrm{C\,min}^{-1}$ to 250, 300, 325, 350, 375, 400 and 450 °C and held for 1 h. Length and width determined from BF-TEM pictures for 50 particles per temperature.
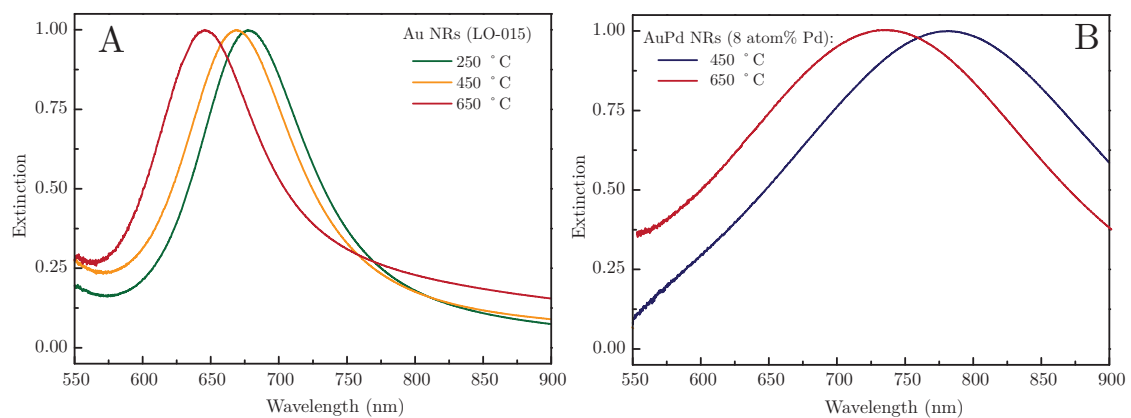

Figure 4.10: Normalized optical absorption spectra of a) Au@mSiO$_2$ NRs heated to 250, 450 and 650 °C and b) AuPd@mSiO$_2$ NRs with 8 atom% heated to 450 and 650 °C. All samples were heated in tube oven in a small glass vial under H$_2$-flow.

Above mentioned experiment was conducted with AuPd@mSiO$_2$ NRs rods which were dopcasted onto a TEM-grid and heated in a tube oven. However during the catalytic tests AuPd NRs@SiO$_2$ (AuPd@mSiO$_2$ NRs on a SiO$_2$ support) were used inside a different oven. The different support medium and oven could have influenced the exact heating temperature of the rods. Therefore, AuPd NRs@SiO$_2$ (8 atom% Pd) were heated in the oven used for the catalytic tests and the degree of alloying was determined per heating temperature, see figure 4.12b. For this experiment the alloying temperature was 373 °C.

4.4.3 Alloying under vacuum: In-situ TEM

In all above mentioned heating experiments the atomic distribution was analysed after the rods had been cooled down. By making use of a heating chip designed for TEM, the alloying could also be followed for the same particle and in real-time.

A mixture of rods with varying Pd content was used for this heating experiment, of which an EDX map prior to heating is shown in figure 4.14a. The three indicated rods, with 6 %, 21 % and 43 atom% Pd as quantified by EDX, were followed as the temperature was increased. In figure 4.13 EDX maps of these rods at each of the different heating temperatures are shown. This figure shows two important features. First, the rod with 43 % Pd had a rough surface before heating. Upon heating the surface smoothed first and later the rod started to alloy. Second, the alloying started at higher temperatures with increasing Pd content. The latter was quantified by making RGB-maps of these three rods at the different heating temperatures. The core- and shell diameter was plotted as a function of heating temperature in figure 4.14b. Once the two lines coincided the core and shell could no longer be distinguished, indicating a completely alloyed rod. Unfortunately the chip could not be heated above 800 °C, so the the rods with 21 % and 43 % Pd were not completely alloyed. The dotted lines, drawn to guide the eye, indicate that a thicker Pd layer indeed resulted in a higher alloying temperature.

4.4.4 Discussion

Particle dimensions were obtained from TEM images of heated NRs and the location of the LSPR peak from absorption spectra gave information about the AR of the rods. Together this showed that the SiO$_2$ shell largely stabilized the rods, as Au NRs with similar AR without SiO$_2$ shell deform severely when heated to 250 °C for 1 h [53]. Once heated to 650 °C the rods started to deform somewhat, and the AuPd@mSiO$_2$ NRs were slightly more stable than Au@mSiO$_2$ NRs. This corresponds to the
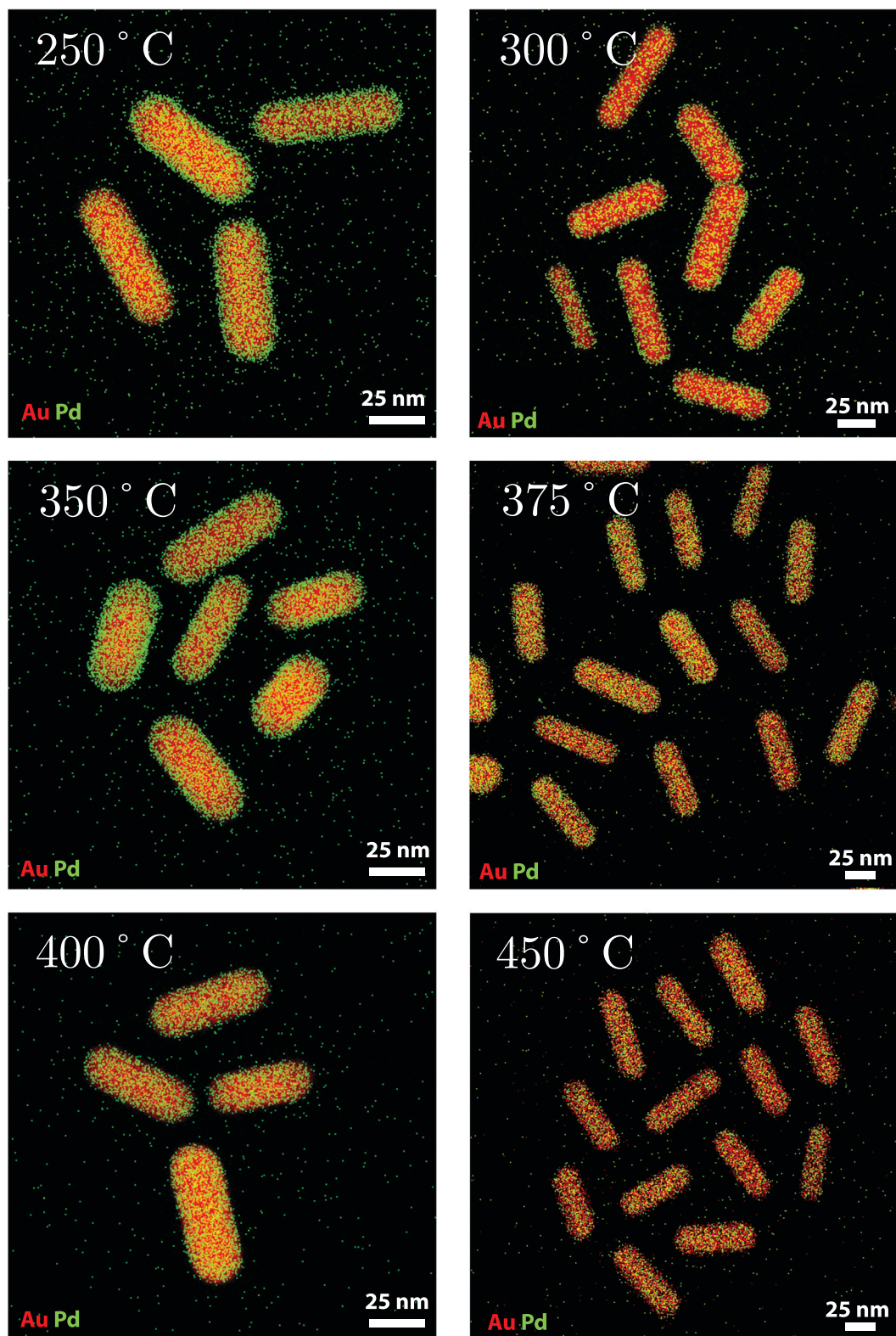
Figure 4.11: EDX maps of AuPd@mSiO$_2$ NRs (8 atom% Pd) heated on a TEM grid to 250, 300, 350, 400 and 450 °C (ramp 2 °C min^{-1}, hold 1 h, H$_2$-flow of ∼100 ml min^{-1}). Red pixels represent Au and green pixels for Pd. Acquisition time was about 10 min.
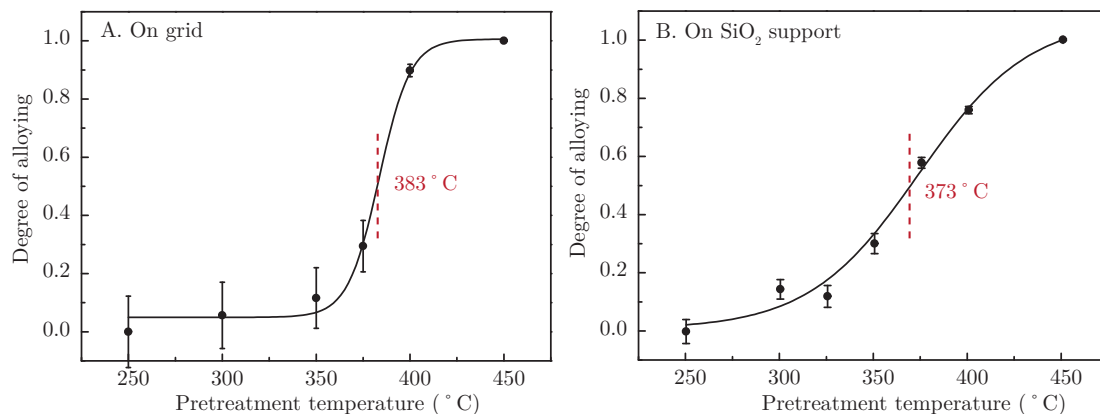
Figure 4.12: Degree of alloying after heating to 250, 300, 350, 375, 400 and 450 °C of a) AuPd@mSiO$_2$ NRs heated on a TEM-grid and b) AuPd NRs@SiO$_2$ supported rods heated inside catalytic set-up. The y-axis represents the degree of alloying, with 0 for the original core-shell and 1 completely alloyed. Degree of alloying as determined from RGB profile plots of EDX maps of 4 particles per heating temperature. See section 3.6.1 for more information about RGB profile plots.

findings of ref [32], where Au@mSiO$_2$ NRs with AR>3 deform upon heating to 700 °C and of ref [18], who found that alloying Au@mSiO$_2$ NRs with a small amount of Pd increased the thermal stability. This could be due to the higher bulk melting point of Pd compared to Au (T_m=1554 °C and T_m=1064 °C) [54].

The alloying process of AuPd NRs with 8 atom% Pd was followed by elemental mapping with HAADF-STEM/EDX, both for rods deposited on TEM grids and SiO$_2$ support. The obtained alloying temperatures from both experiments (383 °C and 373 °C respectively) are comparable, indicating that the determined metal distributions were also present when the differently pretreated rods were used for catalysis. The transition from core-shell to fully alloyed shows that the atomic distribution of bimetallic AuPd NRs@SiO$_2$ could gradually be changed via thermal treatment. This was also observed by [18] for AuAg, AuPt and AuPd NRs for and in more detail by ref [19] for AuAg@mSiO$_2$ NRs. Van der Hoeven *et al.* showed that the alloying temperature in AuAg@mSiO$_2$ NRs depended on several factors, among which the volume of the rod and silver fraction (X_{ag}). In their oven heating experiments under H$_2$ flow, the alloying temperature varied from 305 °C to 375 °C for rods with X_{ag}=0.17 to X_{ag}=0.72. Our alloying temperature of AuPd@mSiO$_2$ NRs lies thus within the same range. However, for AuPd@mSiO$_2$ NRs with X_{Pd}=0.08 (8 atom% Pd), the alloying temperature was higher than that of AuAg NRs with the lowest X_{ag} of 0.17, which could be due to the higher T_m of Pd compared to Au. As pointed out by van der Hoeven *et al.*, other factors beside melting temperature,
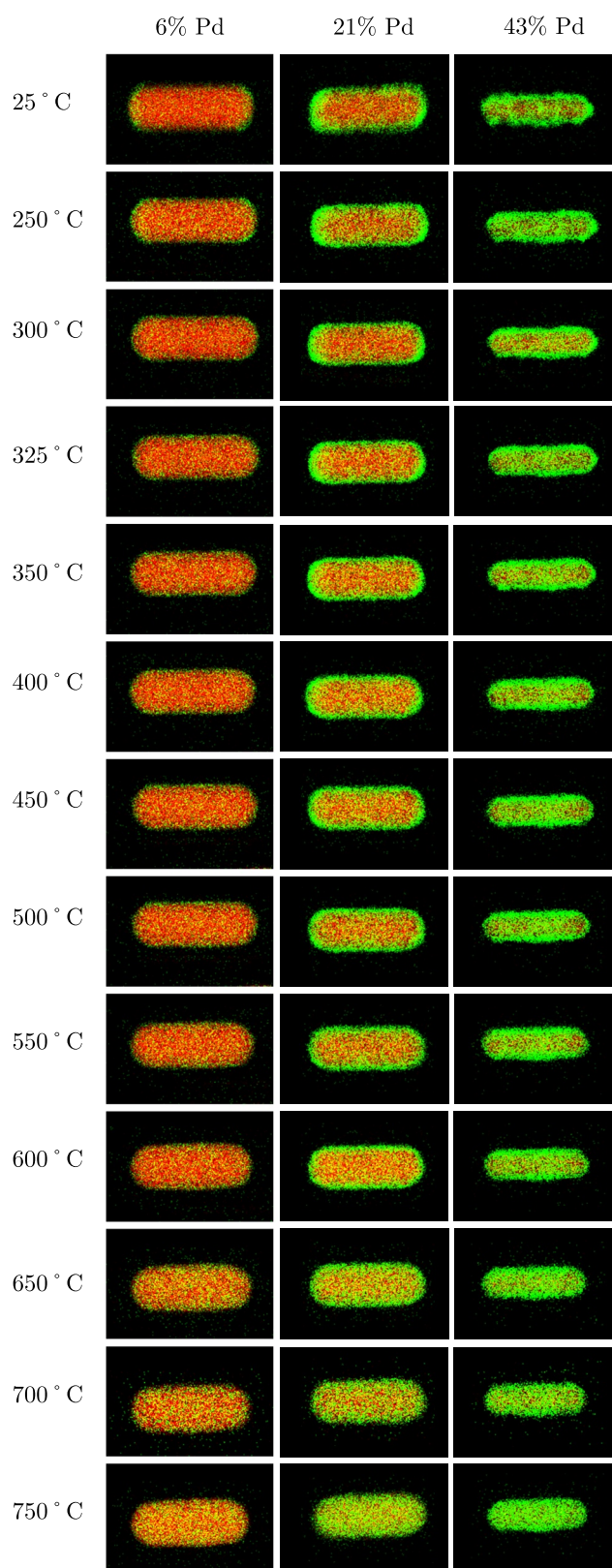
Figure 4.13: EDX maps of AuPd@mSiO$_2$ NRs with in the columns 6, 21, and 43 atom %
Pd (quantified by EDX). Recorded during *in-situ* heating on a SiNx Wildfire heating chip
at 250, 300, 325, 350, 400, 450, 500, 550, 600, 650, 700 and 750 °C, as shown per row.
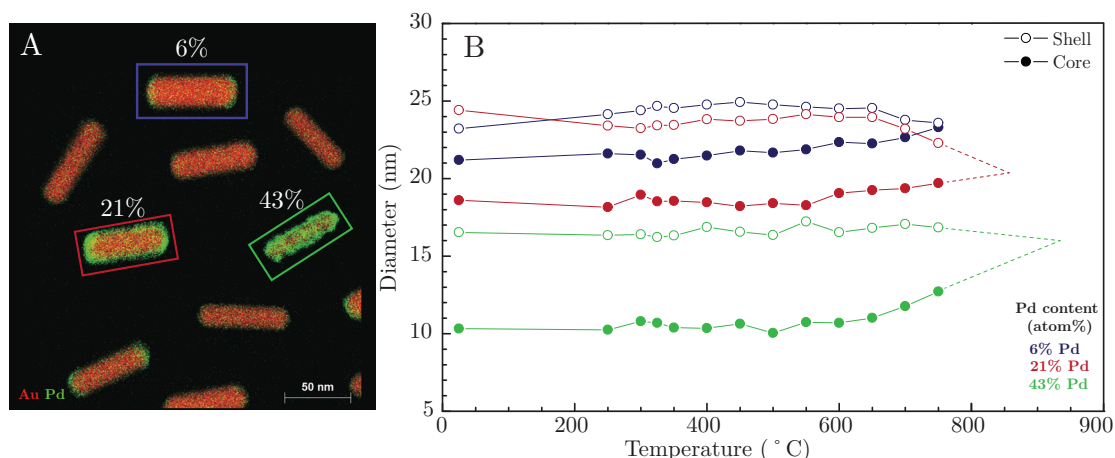The probe current was 700 pA.

Figure 4.14: EDX map of a mixture of AuPd@mSiO$_2$ NRs with different Pd content before heating. Highlighted in blue= 6 atom%, red= 21 atom% and green= 43 atom%. b) Core and shell diameter of AuPd@mSiO$_2$ NRs with 6, 21 and 43 atom%Pd content during heating on heating chip in FEI Talos F200X electron microscope. Core- and shell diameter was determined from EDX maps while kept at 250, 300, 325, 350, 400, 450, 500, 550, 600, 650, 700 and 750 °C. Displayed temperatures do not represent actual ones due to large variations in the heating chip.

such as concentration dependant activation energy for alloying can be more relevant. Unfortunately, no values for activation energy Pd diffusion in Au and vice versa were found in literature for this temperature range.

The heating temperatures during the *in-situ* TEM experiments the were much higher than those found from during the *ex-situ* oven heating. This could be due to the fact that the displayed temperature of the chip was most likely lower than the actual heating temperature. Such temperature deviations on heating chips have also been observed in ref [55] and ref [56]. Furthermore, the rods were heated in vacuum and not under a H$_2$ atmosphere, which was used during pre-treatment for catalysis. Since the gas atmosphere can influence the alloying and deformation process [18], these results are not completely representative. Deviations in alloying temperature with determined from different techniques for AuAg@mSiO$_2$ NRs have also been observed previously in ref [19], where the alloying temperatures determined via *in-situ* TEM-heating and *ex-situ* oven heating measurements was about 80 °C. However, the *in-situ* TEM heating experiment did show that the alloying greatly depended on the amount of Pd present in the rods. The influence of the amount of shell metal on the alloying temperature was also observed in [19]. Here AuAg@mSiO$_2$ with X_{ag} from 0.17 to 0.72 caused the alloying temperature to change from 305 °C to 375 °C. Finally, smoothing of the Pd layer before the rod started to alloy indicates that even core-shell AuPd@mSiO$_2$ NRs with a thick Pd shell pretreated at 250 °C, had a smooth shell when used for the catalytic tests.

4.5 Catalytic tests

The results from the catalytic tests is divided in two sections. First, the influence of a changing atomic distribution is discussed. Second, the effect of the Pd shell thickness is shown.

4.5.1 The atomic distribution

For the study of the influence of atomic distribution of Au and Pd atoms, AuPd NRs@SiO$_2$ with 8 atom% Pd were used (see also table 3.2a). The concentrations of reactants and products as determined by GC for NRs pretreated at seven different temperatures, can be found in figure 4.15. From this the catalytic activity and selectivity was determined.

TOFs for rods with different pretreatment temperatures are shown in figure 4.16a. This figure directly reveals a general trend; a higher pretreatment temperature resulted in lower catalytic activity. In figure 4.16b the TOF at a reaction temperature of 150 °C is shown. As the rods started to alloy more, the TOF reduced from 26 to 1 s^{-1}. In figure 4.16c the selectivity was plotted as a function of the 1,3-butadiene conversion. For rods pretreated at 250-450 °C the selectivity became less as the rods were more alloyed. Figure 4.16d, where the selectivity was plot while at 75 % butadiene conversion, which was the maximum conversion that all of the samples reached, highlights this trend.

Not only the activity and selectivity were influenced by the atomic distribution. The ratio between the 2-butene isomers (1-butene, c-butene and t-butene) also changed. The different isomer fractions are shown in figure 4.17, for a reaction temperature of 225 °C. At this point the reactions are all at about 75 % conversion. This plot shows that for core-shell AuPd NRs@SiO$_2$ the butene ratio was 1-butene>trans-butene>cis-butene, whilst for the alloyed rods this was trans-butene>1-butene>cis-butene. Or quantitatively; a change of the cis:trans from 0.26 to 0.38 when alloying the rods.

4.5.2 Pd shell thickness

To study the influence of the Pd-shell thickness, AuPd NRs@SiO$_2$ with 4, 8, 21, 32 % Pd, Au NRs@SiO$_2$ and a Pd NP@SiO$_2$ reference were compared. An overview of the experiment is shown in table 3.2b. The concentrations of reactants and products as determined by GC for these different AuPd NRs@SiO$_2$ are shown in figure 4.19. The activity and selectivity was calculated from these measurements in the same way as in section 4.5.1. In figure 4.20a the TOF was plot for NRs varying from 0-32 % Pd
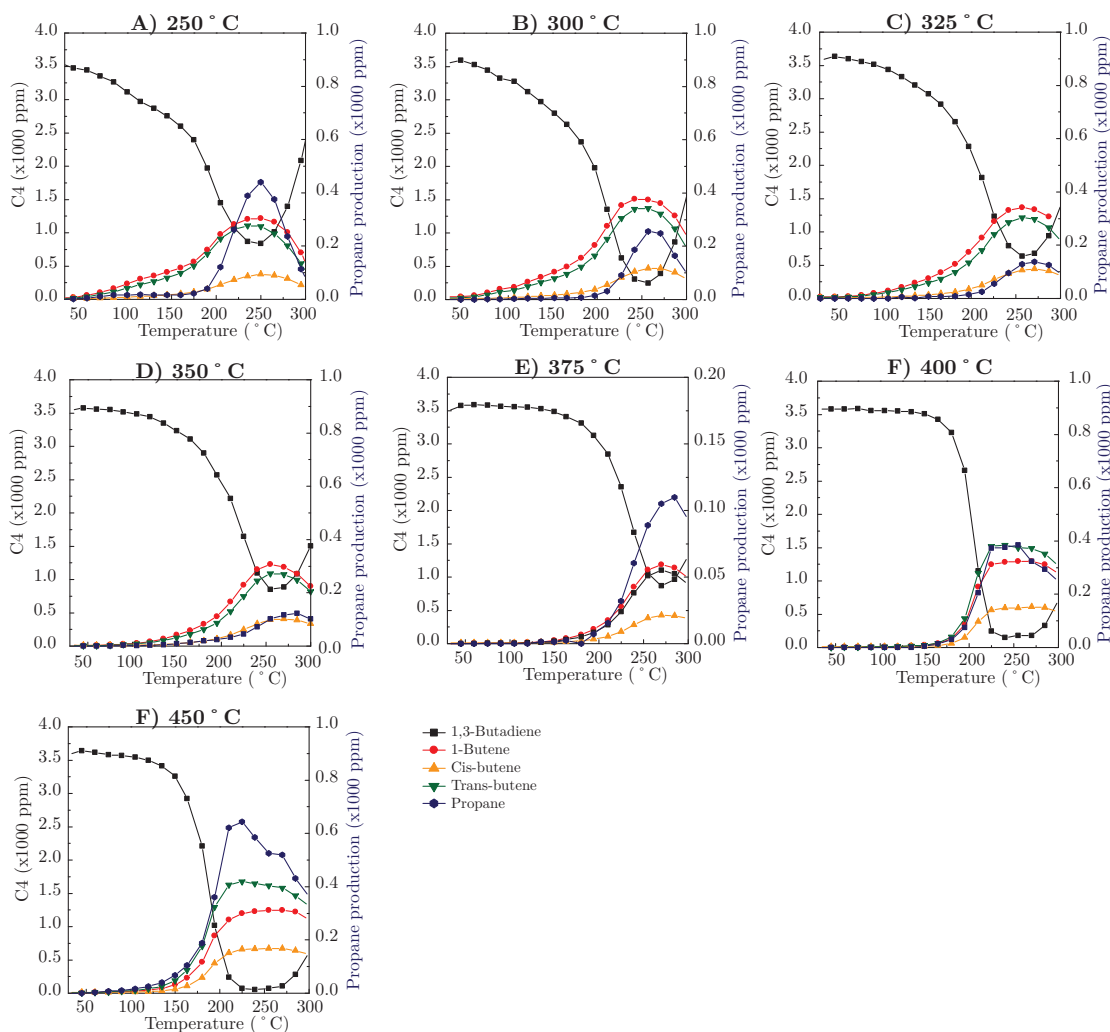
Figure 4.15: Concentrations of reactants and products for AuPd NRs@SiO$_2$ heated to different temperatures and with varying loading. A) 250 °C 20 mg 0.02 wt% , B) 300 °C 20 mg 0.02 wt%, C) 325 °C 20 mg 0.02 wt% , D) 350 °C 20 mg 0.04 wt%, E) 375 °C 20 mg 0.07 wt%, F) 400 °C 20 mg 0.17 wt%, G) 450 °C 40 mg 0.1 wt%

and the Pd NP reference as a function of reaction temperature. In figure 4.20b the TOF at 150 °C is shown. AuPd NRs@SiO$_2$ with 8 %Pd, or 2 atomic layers, gave the highest TOF of 15 s^{-1} compared to 3.9 × 10^{-3}, 1.3, 15, 13, 7.4 and 1.2 s^{-1} of 0, 1, 2, 5 and 8 layers respectively. In figure 4.20c the selectivity as a function of butadiene conversion and in figure 4.20d the selectivity at 97 % butadiene conversion is shown. The selectivity was plot at the highest conversion that all samples reached, since the selectivity can become much worse if the butadiene concentration is low and not all active sites are occupied [47]. The selectivity of the Au NRs was not shown as the conversion was too low. The NRs with one layer of Pd are the most selective and with increasing Pd layers this in general becomes less.
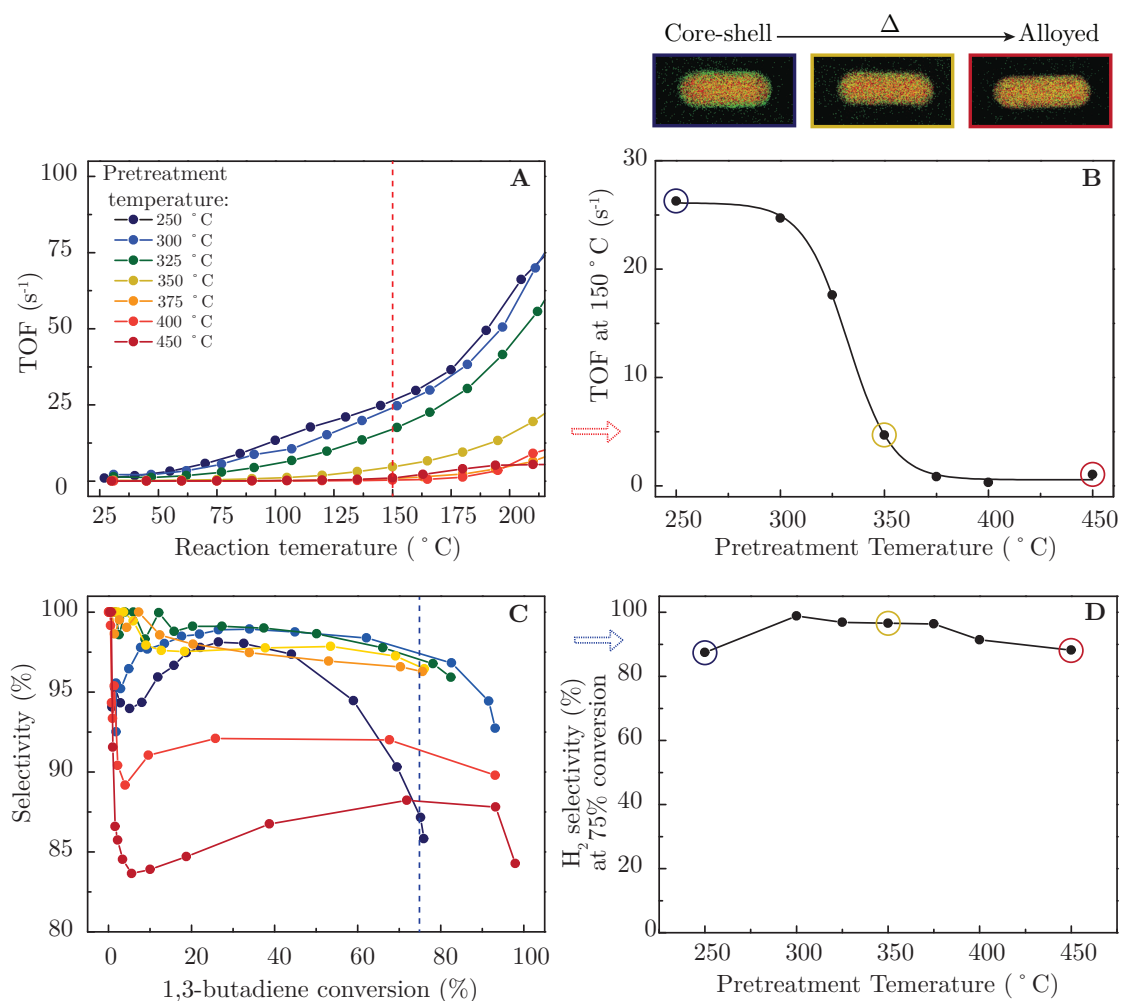
Figure 4.16: a) TOF obtained from AuPd NRs@SiO$_2$ pretreated at different temperatures, for a reaction temperature of 30-250 °C. b) TOF at a reaction temperature of 150 °C. With EDX maps from *ex-situ* experiments of the NRs heated to 250, 350 and 450 °C. c) Selectivity plotted as a function of butadiene conversion d) Selectivity at 75 % butadiene conversion. All AuPd NRs@SiO$_2$ with 8 %Pd, pretreated at 250, 300, 325, 350, 375, 400 and 450 °C, see table 3.2 for used loadings. TOF=turn over frequency in terms of converted 1,3-butadiene molecules per surface atom.

The cis-butene, trans-butene and 1-butene product fractions at a reaction temperature of 225 °C, with core-shell AuPd NRs@SiO$_2$ with 4, 8, 21 and 32 % Pd and Pd NPs@SiO$_2$ reference pretreated at 250 °C and Au NRs@SiO$_2$ are shown in figure 4.18. For Au NRs 1-butene was the most dominant product, which changes to trans-butene upon increasing the Pd shell thickness.
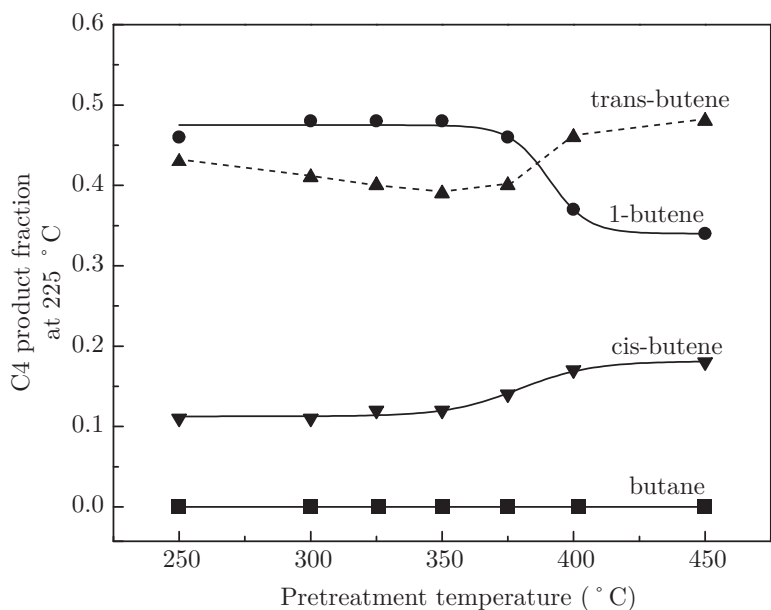
Figure 4.17: Cis-butene, trans-butene, 1-butene and 1-butane product fractions at a reaction temperature of 225 °C for AuPd NRs@SiO$_2$ with 8% Pd pretreated at different temperatures. Solid line=fitted curve and dashed line=drawn to guide the eye.
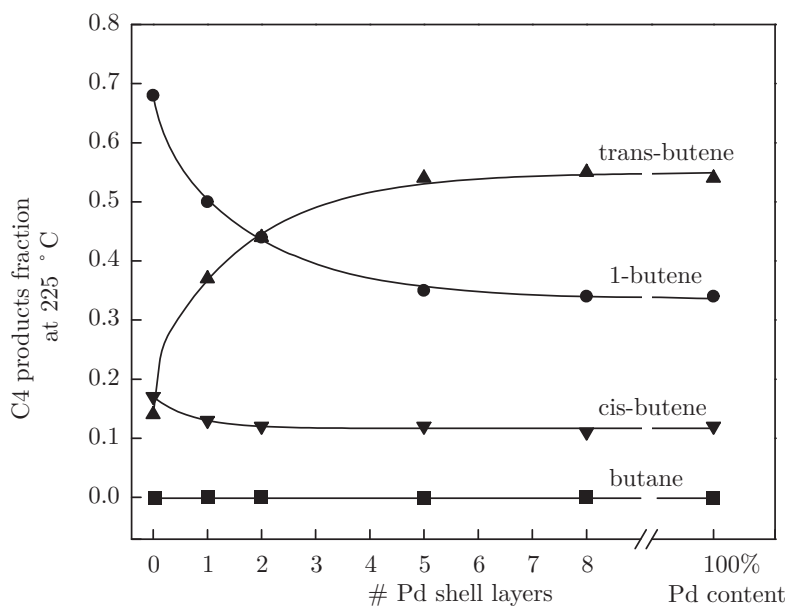

Figure 4.18: Cis-butene, trans-butene and 1-butene product fractions at a reaction temperature of 225 °C, with core-shell AuPd NRs@SiO$_2$ with 4, 8, 21 and 32 atom% Pd and Pd NPs@SiO$_2$ reference pretreated at 250 °C and Au NRs@SiO$_2$.
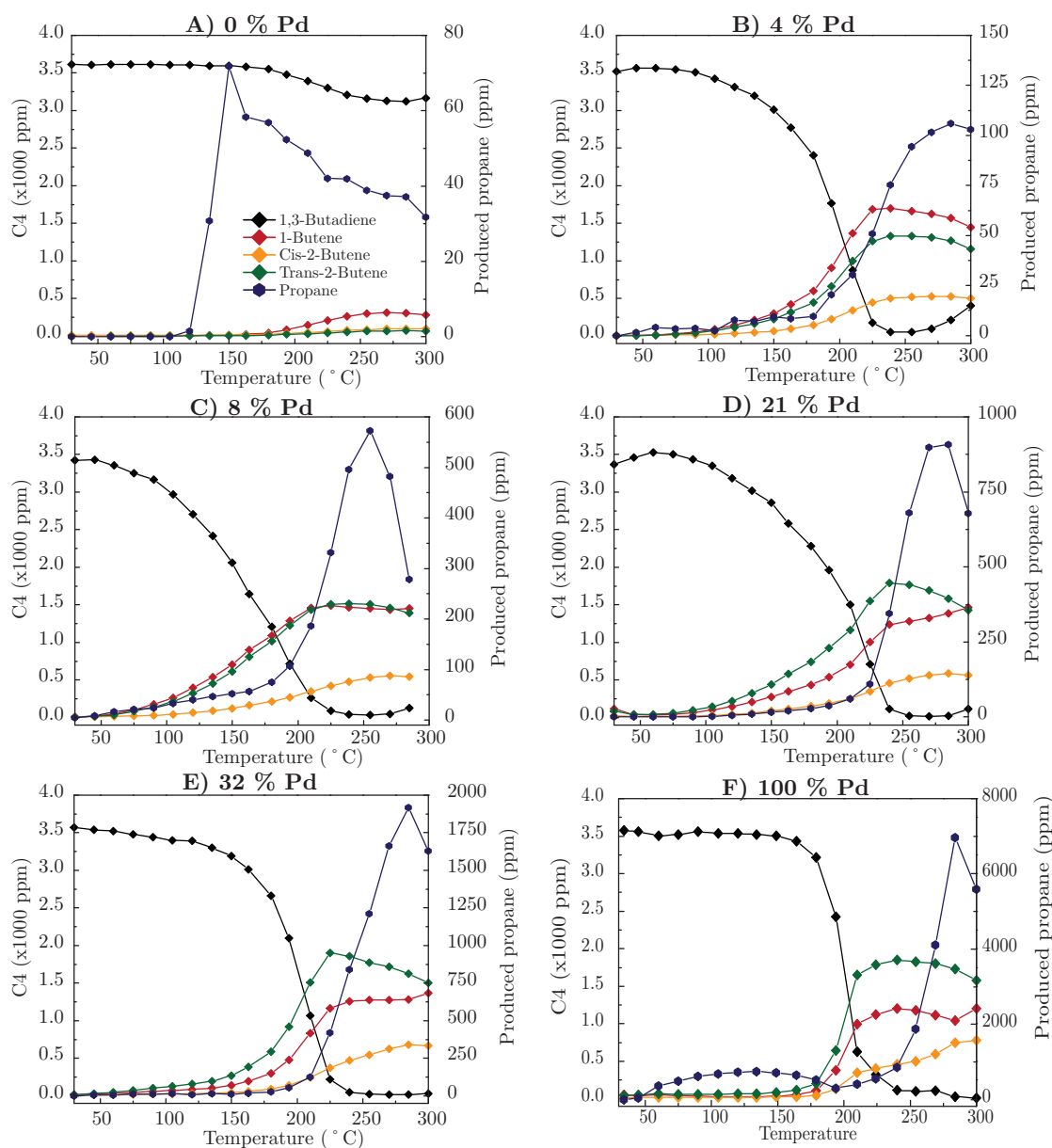
Figure 4.19: Concentrations of reactants and products for AuPd NRs@SiO$_2$ with 4, 8, 21 and 32 %Pd (B-E), Au NRs@SiO$_2$ (A) and Pd NPs@SiO$_2$ reference (F). Reduced under 50 mL H$_2$ at 300 °C (A) and 250 °C (B-F). A) 70 mg 1 wt%, B) 30 mg 0.2 wt%, C) 30 mg 0.04 wt%, D) 30 mg 0.02 wt%, E) 30 mg 0.02 wt%, F) 30 mg 6 × 10^{-3} wt%
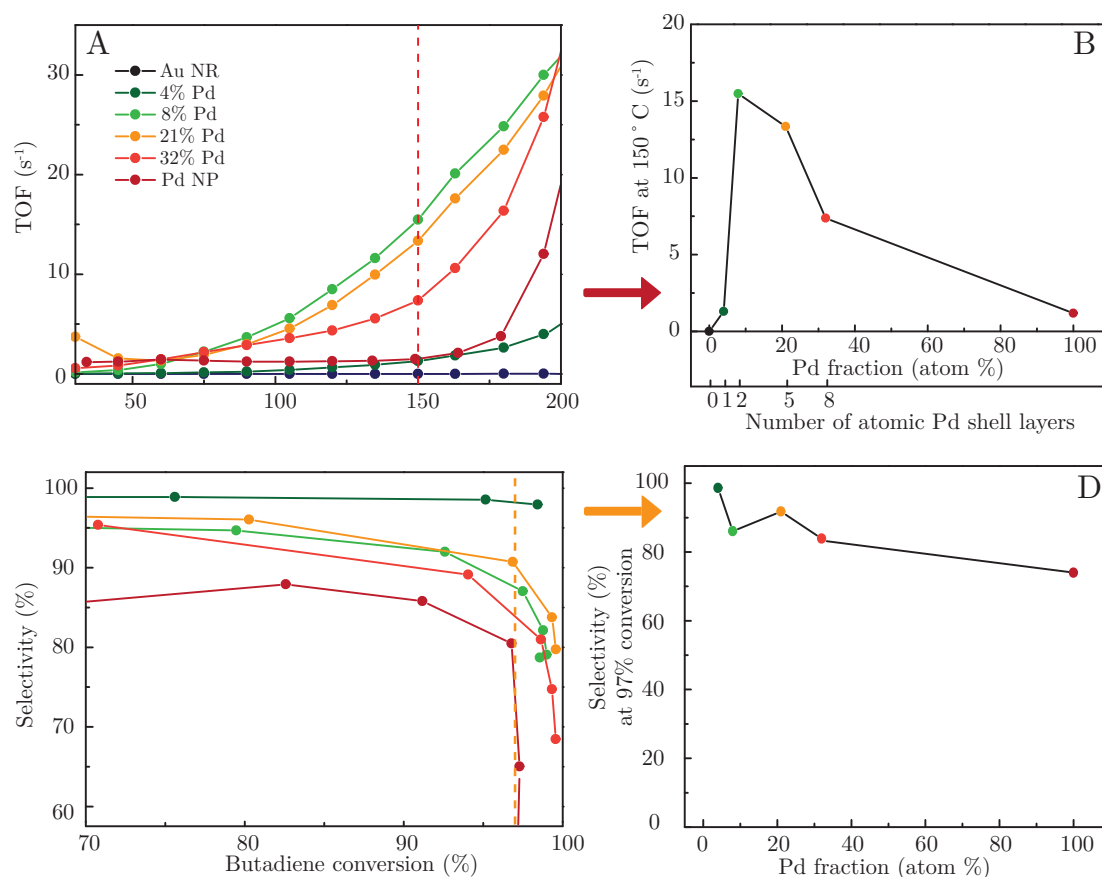
Figure 4.20: a) TOF obtained from core-shell NRs with varying Pd sbell thickness for reaction temperatures of 30-250 °C. b) TOF at a reaction temperature of 150 °C from (a). c) H_2 selectivity plotted as a function of butadiene conversion. d) H_2-selectivity at 97 % butadiene conversion. AuPd@SiO$_2$ NRs with 4, 8, 21 and 32 %Pd and Pd NPs@SiO$_2$ reference, pretreated at 250 °C. In a+b also Au NRs. See table 3.2 for used loadings. TOF=turn over frequency in terms of converted 1,3-butadiene molecules per surface atom. H_2 selectivity in terms of H_2 used to form butene products compared to all used H_2

4.5.3 Discussion

The alloying changes the surface of the rods from entirely covered by Pd atoms to a mix of Pd and Au atoms. Since Au is much less active in the hydrogenation reaction, due to it's limit ability to split H_2 [57], it was expected that activity decreases upon alloying, which was also observed. However, the activity remained constant for rods pretreated at $\geq 375\,°C$, which corresponded to the alloying temperature of $383\,°C$, as determined from the oven heating experiments. It appears that only the change from core-shell to partially alloyed (core-to-shell ratio = 0.5) significantly influenced the catalytic activity, while the change from partially alloyed to fully alloyed did not.

At $60\,°C$ the maximum TOF was $3.7\,s^{-1}$, which reduced to $0.06\,s^{-1}$ upon alloying. The most active AuPd bimetallic catalyst with $5\,\%$ Pd of Kolli *et al.*, reached a TOF of $0.1\,s^{-1}$ at this temperature. Other samples with $5\,\%$ Pd had a TOF of $7.4 \times 10^{-3}\,s^{-1}$ [15]. This implies that our core-shell rods were very active and even the alloyed structures performed very well. At the highest conversion level ($75\,\%$ for the rods with $8\,\%$ Pd), the selectivity varied between 87-$98\,\%$, whilst the most active bimetallic particles of Kolli *et al.* were $\sim 50\,\%$ selective. This selectivity was estimated from the published graphs and by making use of the same selectivity definition used in this thesis. The core-shell structure of the rods thus allowed high conversion while maintaining a high selectivity.

The fact that the selectivity appeared to become less for alloyed rods was unexpected. Due to the alloying the surface contained more Au atoms, and Au itself should in principle be much more selective than Pd [14]. There are however many reports where the catalytic properties of AuPd alloys significantly differs from its monometallic counterparts [58–60]. This phenomena is often ascribed to ligand and ensemble effects and lattice strain [61–63]. The ensemble effect describes the dilution of a surface, so in our case neighbouring Pd ensembles are replaced by Pd islands, which results in a different geometric orientation. Ligand effects are electronic disturbances; they arise when charge transfer between two atoms occurs, affecting the catalytic properties. This can for example result in a change of the filling of the d-band, which affects the adsorption strength of reactants and products on Pd surface atoms [61, 64]. Both ligand and ensemble effects occur simultaneously, and are most likely together responsible for the change in activity and selectivity.

The presence of neighbouring Pd sites in AuPd nanoparticles can either have a positive of negative effect on its catalytic properties, depending on the reaction. For example, Wei *et al* showed that Pd ensembles were needed in the decomposition of N_2O because they acted as the active site [65]. On the other hand, in the hydrogenation of aromatics,. AuPd alloy samples had an increased activity compared

to the sample with separate Au and Pd phases [59]. The authors ascribed this to geometric effects due to Pd ensemble dilution in the AuPd alloy. Also, in the selective oxidation of glycerol, particles with Pd atoms isolated by Au atoms resulted in a more active catalyst [66]. Kolli *et al.* reason that their high selectivity in the selective hydrogenation of butadiene with AuPd was caused by the absence of Pd ensembles [15]. However, they do assume that the AuPd particles do not restructure under H_2 meaning that Pd ensembles were not formed. Yet, our core-shell rods were even more selective than the alloyed ones, which indicates that Pd-ensembles were more active in this reaction. As explained further in this section, electronic effects can also largely influence the catalytic properties, so the exact role of these geometric effects is unknown. Furtermore, upon alloying the NRs, the main product changed from 1-butene to trans-butene, and the cis:trans ratio increased (figure 4.17). This could be due to isolated Pd-atoms in the alloyed rods, since cis-butene intermediates are more stable when adsorbed on isolated Pd atoms than on Pd ensembles [50].

Besides ligand and ensemble effects, lattice strain can also influence the catalytic properties [62, 63]. In ref [62] and [63] lattice strain was even explored as a means to control electrochemical catalytic performance. Wang *et al.* showed that for Pt on Pd core-shell icosahedra in a oxygen reduction reaction an average of 2.7 layers performs 7 times better than a commercial available catalyst, which they ascribe to a compressed lattice of Pt due to Pd[67]. Pt on Pd leads to a lattice mismatch of less than 1 %. Pd and Au have a lattice mismatch of about 4 % (3.89 vs 4.08 Å)[68]. This seemingly small mismatch could thus possible already affect the catalytic properties of the rods.

The influence of ligand, ensemble and lattice strain effects became even clearer from the experiments with core-shell AuPd NRs@SiO_2 with a Pd shell of 1-8 layers thick (figure 4.20b,d). The maximum activity and selectivity was reached for rods with 8 % Pd (2 two atomic layers) and a thicker shell only resulted in lower activity. At one atomic layer the activity was also relatively low, but here the Pd layer probably did not yet completely cover the gold, causing the surface structure to resemble more that of an alloyed NR. This volcano-like dependency of the number of Pd layers on the activity is probably due to a d-band shift. The d-band is affected by the amount of Pd-layers in two ways. First, through disturbance of the 3d electrons of the Pd-shell by charge transfer from Au. This disturbance was investigated experimentally for spherical Au-core NPs with increasing Pd-shell layers by Wang *et al.* [69]. With X-ray Photoelectron Spectroscopy (XPS) measurements they showed that adding Pd layers to Au negatively shifts the Pd 3d binding energy. This means that Pd gains electrons from Au, which is counterintuitive since Au is

more electronegative than Pd. However, in AuPd bimetallic systems, Au gains s, p electrons and loses d electrons and vice versa for Pd [70, 71]. For Pd, gaining d-electrons shifts the d-band center away from the Fermi level, which weakens the interaction between adsorbates and the Pd surface, affecting the catalytic properties [61]. Wang *et al.* also showed that as the shell became thicker, the negative shift was reduced. Second, through lattice mismatch between Au and Pd; the Pd-Pd bond length increases when grown on a Au surface. This causes narrowing of the Pd d-band [72]. In this way the interplay of charge transfer and bond length on the d-band explains our volcano-like relationship between Pd layers and activity.

At a certain thickness, the electronic effect of Au on Pd is lost. In the XPS measurements of Wang et al. hardly no effect could be measured for a shell of 1.75 nm and the review of Gilroy *et al.* states that for core-shell NPs with shells thicker than 1.50 nm, or about 6 atomic layers, the electronic coupling is lost [73]. Since our Pd reference sample is less active than the rods with 8 layers, either the electronic coupling is not yet completely gone or other factors such as surface facets, particle size and synthesis method of the reference caused its low activity [74]. The high activity of the core-shell rods can also not be completely ascribed to the bimetallic character of the rods, since the lengths of the rods (which formed ∼70 % of the surface) consisted of Pd {110} facets. Pd {110} facets are 10 × more active than Pd{111} [75]

Next to activity and selectivity, the product selectivity was also dependant on the structure of the rods. For Au NRs the main product was 1-butene, which upon increasing the Pd shell switched to trans-butene (figure 4.18). The Pd-reference also produced trans-butene as the main product. Monometallic Pd generally also gives trans-butene as the major 2-butene product, while for Au NP catalysts cis-butene is the most dominant fraction [76, 77]. As explained in section 2.6, the rate of 1-butene formation decreases upon lowering the d-band Pd. This corresponds very well to reasoning above, which explained that the d-band shifts downward with when increasing the amount of Pd layers on Au.

As shown in figure 4.15 and 4.19, the butadiene conversion significantly dropped at a reaction temperature of about 250 °C during almost all runs. The cause is unknown, but it could be due to formation of carbon deposits on the Pd surface, of which Pd is known to suffer during hydrogenation reactions [8].

A final point of remark regards the use of Ag in the synthesis of the Au NRs. AgNO$_3$ is needed to break symmetry and initiate the growth of rod shaped NP. ICP results showed that the final rods contained about 1 atom% Ag. In industry Ag is used to promote the selectivity of Pd catalysts for selective hydrogenation

of di-alkenes [3]. It is unknown whether the Ag-atoms are close to the surface in our AuPd NRs@SiO$_2$ after growing the Pd-shell and to what extent they influenced the selectivity.

4.5.4 Factors influencing catalytic properties

All experiments discussed in this chapter were performed with the same propene N2.5 bottle of Linde. However, some runs were done with a higher purity bottle of propene (N3.5 of Air Liquide), of which the data was not shown in this thesis. These experiments showed a higher activity than with the lower grade propene. Possibly some contaminants poison the catalyst, reducing it's activity. As the propene 2.5N bottle became more empty, the catalysts were also less active. The precise cause of this is unknown, but could be due to an increased concentration of contaminants in the bottle.

Furthermore, the rods were significantly less active after longer exposure to sunlight. It thus of great importance to perform the entire experiment in a reactor kept away from sunlight and store the samples in the dark, to prevent oxidation of the rods.

5
Conclusions

Via a colloidal seeded method, monodisperse, single crystalline Au nanorods with an average diameter of 20.6±2.3 nm and length of 65±6.3 nm were synthesized. These rods were coated with a mesoporous SiO_2 shell of about 17 nm. By increasing the amount of Pd-precursor (Na_2PdCl_4), increasingly thicker Pd layers were grown on the Au core, where the SiO_2 shell acted as a mould. This resulted in AuPd@mSiO_2 NRs with 2, 4, 8 and 21 atom% Pd. To grow an even thicker layer of Pd, the Au cores were etched in a solution of HCl with H_2O_2 as an oxidant. The length of the rods was successfully decreased by about 12 %, whereas the diameter of the rods stayed approximately the same. Subsequent Pd deposition onto these etched Au cores resulted in AuPd@mSiO_2 NRs with 32 atom% Pd. Via this method we thus successfully made AuPd@mSiO_2 NRs with 1, 2, 5 and 8 atomic layers of Pd. All the rods also contained about 1 atom% Ag, which could not be removed by washing in a solution of NH_3 and H_2O_2. This location of this Ag in the finished AuPd@mSiO_2 NRs is however unknown.

Next, the alloying behaviour of AuPd@mSiO_2 NRs with 8 atom% Pd was characterised. This was done by heating the rods under a H_2 flow to different temperatures while deposited onto a TEM-grid, after which the metal distribution was analysed with HAAFD-STEM/EDX. From the EDX maps the core- and shell diameter at each of the heating temperatures was determined. The experiment was repeated with rods deposited onto SiO_2 support to match the conditions used during H_2 pretreatment for catalytic tests. The alloying temperature of both methods were similar; 373 °C) and 383 °C for rods on SiO_2 support and a TEM grid respectively. This showed that the atomic distribution could be controlled from

core-shell to partially alloyed to fully alloyed by varying the heating temperature from 250 °C to 450 °C. The found alloying temperature is comparable to those found for AuAg@mSiO$_2$. During the heat treatment needed to induce the alloying, the rods did not deform, which was indicated by TEM-imaging and absorption spectroscopy. The metal distribution was thus the only parameter changed.

AuPd NRs@SiO$_2$ with 8 atom% were used to catalyse the selective hydrogenation of 1,3-butadiene in an excess of propene. The rods were pretreated under H$_2$ at different temperatures from 250-450 °C, ensuring that the atomic distribution gradually varied from core-shell to fully alloyed. The Turn Over Frequency (TOF) at a reaction temperature of 150 °C reduced from 26 to 0.30 s^{-1} as the rods were more alloyed, while the selectivity remained high (>88 %). This activity and selectivity of the core-shell rods was higher than that of previously published alloyed AuPd NPs under the same reaction conditions. The decreased activity upon alloying could be explained as a result of less Pd atoms at the surface. However since the selectivity remained high for all structures, electronic influences of Au on Pd caused by ligand, ensemble and lattice strain effects, must have also played a role.

The influence of ligand, ensemble and lattice strain effects became even more clear in the experiments where the Pd shell thickness was varied. AuPd NRs@SiO$_2$ with 8 atom% Pd, which corresponded to two atomic layers, gave the highest activity. A thicker Pd shell only lowered the activity. The different butene isomer fractions also depended on thickness of the Pd shell; with increasing Pd content, the main product changed from 1-butene to trans-butene. Since no Au atoms were at the surface, the Au core must thus have electronically influenced Pd shell atoms. This change in catalytic activity could have been due to a shift of the Pd d-band, which was explained by ligand and ensemble effects but also by lattice strain. The changed product selectivity could also be related to this shift of the d-band.

Both the experiments with varying atomic distribution and varying Pd shell thickness showed the significant importance of the atomic distribution on catalytic performance, indicating that the performance of bimetallic catalysts can further be optimized via the metal distribution.

6
Outlook

This work showed the influence of atomic distribution in AuPd bimetallic NRs on the catalytic behaviour in the selective hydrogenation of butadiene. For all experiments rods with approximately the same volume and aspect ratio were used. It would be interesting to extend this research to rods with different ARs, as this would also change the ratio between which facets are exposed and could provide more information on what role these facets play in the obtained high activities.

Furthermore, by varying the 1,3-butadiene concentration the order of the reaction and thus more kinetic information can be obtained, for example regarding the activation energy of the differently structured AuPd NRs@SiO$_2$. Also, as briefly discussed in section 4.5.4, the catalytic properties appeared to be largely influenced by the purity of the propene gas that was used. It would therefore be useful to repeat some of the experiments with high purity grade propene.

Pd was chosen as shell material since the combination of Au and Pd is known to be very active with high a selectivity for this selective hydrogenation reaction. Bimetallic AuCu particles are however also promising for this reaction. Copper catalysts itself have a relatively high activity and selectivity [**Koeppel1994**], but they deactivate quickly due to oligomerisation [**OSSIPOFF1994**]. In the selective hydrogenation of butadiene Delannoy *et al.* showed that bimetallic AuCu catalysts were more active than Au and had a different selectivity towards 2-butenes than monometallic copper and gold [78]. A Cu shell grown on the Au core could therefore also provide more information on how the atomic distribution influences the catalytic properties and whether the Au core can also influence a Cu shell so significantly as Au does for Pd.

Since the attempt to remove Ag from the rods proved unsuccessful, the influence of Ag on the catalytic properties of our AuPd NRs@SiO$_2$ remains unknown. It would therefore be useful to introduce some extra Ag into the rods, and investigate whether this affects the selectivity.

Finally, all experiments had a drop in activity at around 250 °C. This could be due several factors, but it is most likely caused by carbon deposition on the metal surface. This hypothesis could be tested by flushing with some O$_2$ after the drop, which should burn of the deposited hydrocarbons.

Acknowledgements

References

(1)   Derrien, M. L. Selective Hydrogenation Applied to the Refining of Petrochemical Raw Materials Produced by Steam Cracking. *Studies in Surface Science and Catalysis* **1986**, *27*, 613–666.

(2)   Johnson, M. M.; Walker, D. W.; Nowack, G. P. Selective hydrogenation catalyst. *U.S. Patent, 4,404,124* **1983**.

(3)   Frevel, L; Kressley, L Selective hydrogenation of acetylene in ethylene and catalyst therefor. *U.S. Patent, 2,802,889* **1957**.

(4)   Bates, A. J.; Leszczynski, Z. K.; Phillipson, J. J.; Wells, P. B.; Wilson, G. R. The hydrogenation of akladienes. Part IV. The reaction of buta-1,3-diene with deuterium catalysed by rhodium, palladium, and platinum. *Journal of the Chemical Society A: Inorganic, Physical, Theoretical* **1970**, *2*, 2435.

(5)   Tardy, B; Noupa, C; Nihoul, G Catalytic hydrogenation of 1,3-butadiene on Pd particles evaporated on carbonaceous supports: Particle size effect. *Journal of Catalysis* **1991**, *129*, 1–11.

(6)   Molnár, Á.; Sárkány, A.; Varga, M. Hydrogenation of carbon–carbon multiple bonds: chemo-, regio- and stereo-selectivity. *Journal of Molecular Catalysis A: Chemical* **2001**, *173*, 185–221.

(7)   Nikolaev, S. A.; Zanaveskin, L. N.; Smirnov, V. V.; Averyanov, V. A.; Zanaveskin, K. L. Catalytic hydrogenation of alkyne and alkadiene impurities from alkenes. Practical and theoretical aspects. *Russian Chemical Reviews* **2009**, *78*, 231–247.

(8)   McCue, A. J.; Anderson, J. A. Recent advances in selective acetylene hydrogenation using palladium containing catalysts. *Frontiers of Chemical Science and Engineering* **2015**, *9*, 142–153.

(9)   Bond, G. C.; Sermon, P. A.; Webb, G.; Buchanan, D. A.; Wells, P. B. Hydrogenation over supported gold catalysts. *Journal of the Chemical Society, Chemical Communications* **1973**, 444b.

(10)   Okumura, M.; Akita, T.; Haruta, M. Hydrogenation of 1,3-butadiene and of crotonaldehyde over highly dispersed Au catalysts. *Catalysis Today* **2002**, *74*, 265–269.

(11)   Jia, J.; Haraki, K.; Kondo, J. N.; Domen, K.; Tamaru, K. Selective Hydrogenation of Acetylene over Au/Al2O3 Catalyst. *The Journal of Physical Chemistry B* **2000**, *104*, 11153–11156.

(12)   Lopez-Sanchez, J. A.; Lennon, D. The use of titania- and iron oxide-supported gold catalysts for the hydrogenation of propyne. *Applied Catalysis A: General* **2005**, *291*, 230–237.

(13) Juliusa, M.; Robertsa, S.; Fletchera, J. C. Q. A review of the use of gold catalysts in selective hydrogenation reactions. *Gold Bulletin* **2010**, *43*, 298–306.

(14) Hugon, A.; Delannoy, L.; Louis, C. Supported gold catalysts for selective hydrogenation of 1,3-butadiene in the presence of an excess of alkenes. *Gold Bulletin* **2008**, *41*, 127–138.

(15) Kolli, N. E.; Delannoy, L.; Louis, C. Bimetallic Au-Pd catalysts for selective hydrogenation of butadiene: Influence of the preparation method on catalytic properties. *Journal of Catalysis* **2013**, *297*, 79–92.

(16) Hong, J. W.; Kim, D.; Lee, Y. W.; Kim, M.; Kang, S. W.; Han, S. W. Atomic-distribution-dependent electrocatalytic activity of Au-Pd bimetallic nanocrystals. *Angewandte Chemie - International Edition* **2011**, *50*, 8876–8880.

(17) Masoud, N.; Delannoy, L.; Calers, C.; Gallet, J.-J.; Bournel, F.; de Jong, K. P.; Louis, C.; de Jongh, P. E. Silica-Supported Au-Ag Catalysts for the Selective Hydrogenation of Butadiene. *ChemCatChem* **2017**, *9*, 2418–2425.

(18) Albrecht, W.; van der Hoeven, J. E.; Deng, T. S.; de Jongh, P. E.; van Blaaderen, A. Fully alloyed metal nanorods with highly tunable properties. *Nanoscale* **2017**, *9*, 2845–2851.

(19) Van der Hoeven, J. E. S.; Welling, T. A. J.; Silva, T. A. G.; van den Reijen, J. E.; La Fontaine, C.; Carrier, X.; Louis, C.; van Blaaderen, A.; de Jongh, P. E. In Situ Observation of Atomic Redistribution in Alloying Gold–Silver Nanorods. *ACS Nano* **2018**, *12*, 8467–8476.

(20) Lohse, S. E.; Murphy, C. J. The quest for shape control: A history of gold nanorod synthesis. *Chemistry of Materials* **2013**, *25*, 1250–1261.

(21) Huang, X.; Neretina, S.; El-Sayed, M. A. Gold Nanorods: From Synthesis and Properties to Biological and Biomedical Applications. *Advanced Materials* **2009**, *21*, 4880–4910.

(22) Jana, N. R.; Gearheart, L.; Murphy, C. J. Seed-Mediated Growth Approach for Shape-Controlled Synthesis of Spheroidal and Rod-like Gold Nanoparticles Using a Surfactant Template. *Advanced Materials* **2001**, *13*, 1389–1393.

(23) Nikoobakht, B.; El-Sayed, M. A. Preparation and growth mechanism of gold nanorods (NRs) using seed-mediated growth method. *Chemistry of Materials* **2003**, *15*, 1957–1962.

(24) Walsh, M. J.; Barrow, S. J.; Tong, W.; Funston, A. M.; Etheridge, J. Symmetry breaking and silver in gold nanorod growth. *ACS Nano* **2015**, *9*, 715–724.

(25) Almora-Barrios, N.; Novell-Leruth, G.; Whiting, P.; Liz-Marzán, L. M.; López, N. Theoretical description of the role of halides, silver, and surfactants on the structure of gold nanorods. *Nano Letters* **2014**, *14*, 871–875.

(26) Walsh, M. J.; Tong, W.; Katz-Boon, H.; Mulvaney, P.; Etheridge, J.; Funston, A. M. A Mechanism for Symmetry Breaking and Shape Control in Single-Crystal Gold Nanorods. *Accounts of Chemical Research* **2017**, *50*, 2925–2935.

(27) Jackson, S. R.; McBride, J. R.; Rosenthal, S. J.; Wright, D. W. Where's the silver? imaging trace silver coverage on the surface of gold nanorods. *Journal of the American Chemical Society* **2014**, *136*, 5261–5263.

(28) Ye, X.; Zheng, C.; Chen, J.; Gao, Y.; Murray, C. B. Using binary surfactant mixtures to simultaneously improve the dimensional tunability and monodispersity in the seeded growth of gold nanorods. *Nano Letters* **2013**, *13*, 765–771.

(29) Li, W.; Zhang, M.; Zhang, J.; Han, Y. Self-assembly of cetyl trimethylammonium bromide in ethanol-water mixtures. *Frontiers of Chemistry in China* **2006**, *1*, 438–442.

(30) Murphy, C. J.; Sau, T. K.; Gole, A. M.; Orendorff, C. J.; Gao, J.; Gou, L.; Hunyadi, S. E.; Li, T. Anisotropic metal nanoparticles: Synthesis, assembly, and optical applications. *Journal of Physical Chemistry B* **2005**, *109*, 13857–13870.

(31) Lohse, S. E.; Burrows, N. D.; Scarabelli, L.; Liz-Marzán, L. M.; Murphy, C. J. Anisotropic noble metal nanocrystal growth: The role of halides., 2014.

(32) Gergely-Fülöp, E.; Zámbó, D.; Deák, A. Thermal stability of mesoporous silica-coated gold nanorods with different aspect ratios. *Materials Chemistry and Physics* **2014**, *148*, 909–913.

(33) Deng, T.-S.; van der Hoeven, J. E. S.; Yalcin, A. O.; Zandbergen, H. W.; van Huis, M. A.; van Blaaderen, A. Oxidative Etching and Metal Overgrowth of Gold Nanorods within Mesoporous Silica Shells. *Chemistry of Materials* **2015**, *27*, 7196–7203.

(34) Gorelikov, I.; Matsuura, N. Single-step coating of mesoporous silica on cetyltrimethyl ammonium bromide-capped nanoparticles. *Nano Letters* **2008**, *8*, 369–373.

(35) Brinker, C. Hydrolysis and condensation of silicates: Effects on structure. *Journal of Non-Crystalline Solids* **1988**, *100*, 31–50.

(36) Nooney, R. I.; Thirunavukkarasu, D.; Chen, Y.; Josephs, R.; Ostafin, A. E. Self-assembly of mesoporous nanoscale silica/gold composites. *Langmuir* **2003**, *19*, 7628–7637.

(37) Firouzi, A.; Kumar, D.; Bull, L. M.; Besier, T.; Sieger, P.; Huo, Q.; Walker, S. A.; Zasadzinski, J. A.; Glinka, C.; Nicol, J.; Margolese, D.; Stucky, G. D.; Chmelka, B. F. Cooperative organization of inorganic-surfactant and biomimetic assemblies. *Science* **1995**, *267*, 1138–1143.

(38) Link, S.; El-Sayed, M. A. Size and Temperature Dependence of the Plasmon Absorption of Colloidal Gold Nanoparticles. *The Journal of Physical Chemistry B* **1999**, *103*, 4212–4217.

(39) Long, Y.-T.; Jing, C., *Localized Surface Plasmon Resonance Based Nanobiosensors*; Springer: New York, 2014.

(40) Cao, J.; Sun, T.; Grattan, K. T. Gold nanorod-based localized surface plasmon resonance biosensors: A review. *Sensors and Actuators, B: Chemical* **2014**, *195*, 332–351.

(41) Link, S.; El-Sayed, M. A. Spectral Properties and Relaxation Dynamics of Surface Plasmon Electronic Oscillations in Gold and Silver Nanodots and Nanorods. *The Journal of Physical Chemistry B* **1999**, *103*, 8410–8426.

(42) Ali, M. R. K.; Snyder, B.; El-Sayed, M. A. Synthesis and Optical Properties of Small Au Nanorods Using a Seedless Growth Technique. *Langmuir* **2012**, *28*, 9807–9815.

(43) Huang, X.; El-Sayed, I. H.; Qian, W.; El-Sayed, M. A. Cancer Cell Imaging and Photothermal Therapy in the Near-Infrared Region by Using Gold Nanorods. *Journal of the American Chemical Society* **2006**, *128*, 2115–2120.

(44) Zhao, J.; Nguyen, S. C.; Ye, R.; Ye, B.; Weller, H.; Somorjai, G. A.; Alivisatos, A. P.; Dean Toste, F. A Comparison of Photocatalytic Activities of Gold Nanoparticles Following Plasmonic and Interband Excitation and a Strategy for Harnessing Interband Hot Carriers for Solution Phase Photocatalysis. *ACS Central Science* **2017**, *3*, 482–488.

(45) Gu, M.; Li, X.; Lan, T.-H.; Tien, C.-H. Plasmonic keys for ultra-secure information encryption. *SPIE Newsroom* **2012**, DOI: `10.1117/2.1201211.004538`.

(46) Horiuti, J.; Polanyi, M. Outlines of a theory of proton transfer. *Journal of Molecular Catalysis A: Chemical* **2003**, *199*, 185–197.

(47) Anderson, J; Wells, R, *Supported Metals in catalysis*, 2nd; World Scientific: 2012, pp 180–185.

(48) Gaube, J.; Klein, H. F. Kinetics and mechanism of butene isomerization/hydrogenation and of 1,3-butadiene hydrogenation on palladium. *Applied Catalysis A: General* **2014**, *470*, 361–368.

(49) Moyes, R. B.; Wells, P. B.; Grant, J; Salman, N. Y. Electronic effects in butadiene hydrogenation catalysed by the transition metals. *Applied Catalysis A: General* **2002**, *229*, 251–259.

(50) Souza, P. R.; Pereira, M. M.; Antunes, O. A.; Aranda, D. A.; Carneiro, J. W. 1,3-butadiene hydrogenation on Pd-supported systems: Geometric effects. *Brazilian Journal of Chemical Engineering* **2002**, *19*, 187–194.

(51) Bondi, A. van der Waals Volumes and Radii. *The Journal of Physical Chemistry* **1964**, *68*, 441–451.

(52) Okamoto, F. Etching solution for silver. *U.S. Patent, 391,358* **1975**, 1–4.

(53) Petrova, H.; Perez Juste, J.; Pastoriza-Santos, I.; Hartland, G. V.; Liz-Marzán, L. M.; Mulvaney, P. On the temperature stability of gold nanorods: comparison between thermal and ultrafast laser-induced heating. *Phys. Chem. Chem. Phys.* **2006**, *8*, 814–821.

(54) Haynes, W. M., *CRC Handbook of Chemistry and Physics*; CRC Handbook of Chemistry and Physics; CRC Press: 2011, 4–65 and 4–79.

(55) Niekiel, F.; Kraschewski, S. M.; Müller, J.; Butz, B.; Spiecker, E. Local temperature measurement in TEM by parallel beam electron diffraction. *Ultramicroscopy* **2017**, *176*, 161–169.

(56) Van Omme, J. T.; Zakhozheva, M.; Spruit, R. G.; Sholkina, M.; Pérez Garza, H. H. Advanced microheater for in situ transmission electron microscopy; enabling unexplored analytical studies and extreme spatial stability. *Ultramicroscopy* **2018**, *192*, 14–20.

(57) Stobiński, L.; Zommer, L.; Duś, R. Molecular hydrogen interactions with discontinuous and continuous thin gold films. *Applied Surface Science* **1999**, *141*, 319–325.

(58) Besenbacher, F.; Chorkendorff, I.; Clausen, B. S.; Hammer, B.; Molenbroek, A. M.; Nørskov, J. K.; Stensgaard, I. Design of a surface alloy catalyst for steam reforming. *Science* **1998**, *279*, 1913–1915.

(59) Pawelec, B.; Venezia, A.; La Parola, V.; Cano-Serrano, E.; Campos-Martin, J.; Fierro, J. AuPd alloy formation in Au-Pd/Al2O3 catalysts and its role on aromatics hydrogenation. *Applied Surface Science* **2005**, *242*, 380–391.

(60) Samanta, A.; Rajesh, T.; Nandini Devi, R. Confined space synthesis of fully alloyed and sinter-resistant AuPd nanoparticles encapsulated in porous silica. *Journal of Materials Chemistry A* **2014**, *2*, 4398.

(61) Liu, P; Nørskov, J. K. Ligand and ensemble effects in adsorption on alloy surfaces. *Physical Chemistry Chemical Physics* **2001**, *3*, 3814–3818.

(62) Kuo, C.-H.; Lamontagne, L. K.; Brodsky, C. N.; Chou, L.-Y.; Zhuang, J.; Sneed, B. T.; Sheehan, M. K.; Tsung, C.-K. The Effect of Lattice Strain on the Catalytic Properties of Pd Nanocrystals. *ChemSusChem* **2013**, *6*, 1993–2000.

(63) Strasser, P.; Koh, S.; Anniyev, T.; Greeley, J.; More, K.; Yu, C.; Liu, Z.; Kaya, S.; Nordlund, D.; Ogasawara, H.; Toney, M. F.; Nilsson, A. Lattice-strain control of the activity in dealloyed core–shell fuel cell catalysts. *Nature Chemistry* **2010**, *2*, 454–460.

(64) Gao, F.; Goodman, D. W. Pd–Au bimetallic catalysts: understanding alloy effects from planar models and (supported) nanoparticles. *Chemical Society Reviews* **2012**, *41*, 8009.

(65) Wei, X.; Yang, X.-f.; Wang, A.-q.; Li, L.; Liu, X.-y.; Zhang, T.; Mou, C.-y.; Li, J. Bimetallic Au–Pd Alloy Catalysts for N 2 O Decomposition: Effects of Surface Structures on Catalytic Activity. *The Journal of Physical Chemistry C* **2012**, *116*, 6222–6232.

(66) Wang, D.; Villa, A.; Porta, F.; Prati, L.; Su, D. Bimetallic Gold/Palladium Catalysts: Correlation between Nanostructure and Synergistic Effects. *The Journal of Physical Chemistry C* **2008**, *112*, 8617–8622.

(67) Wang, X.; Choi, S. I.; Roling, L. T.; Luo, M.; Ma, C.; Zhang, L.; Chi, M.; Liu, J.; Xie, Z.; Herron, J. A.; Mavrikakis, M.; Xia, Y. Palladium-platinum core-shell icosahedra with substantially enhanced activity and durability towards oxygen reduction. *Nature Communications* **2015**, *6*, 1–8.

(68) Hermann, K, *Crystallography and Surface Structure: An Introduction for Surface Scientists and Nanoscientists*, 2nd; Wiley VCH: 2016, pp 265–266.

(69) Wang, H.; Wang, C.; Yan, H.; Yi, H.; Lu, J. Precisely-controlled synthesis of Au@Pd core-shell bimetallic catalyst via atomic layer deposition for selective oxidation of benzyl alcohol. *Journal of Catalysis* **2015**, *324*, 59–68.

(70) Rodriguez, J. A. Electronic properties of bimetallic surfaces. *Heterogeneous Chemistry Reviews* **1996**, *3*, 17–32.

(71) Lee, Y.-S; Jeon, Y; Chung, Y. D.; Lim, K. Y.; Whang, C. N.; Oh, S.-J Charge Redistribution and Electronic Behavior in Pd-Au Alloy. *The journal of the Korean Physical Society* **2000**, *37*, 451–455.

(72) Deville, J; Hanbücken, M., *Stress and Strain in Epitaxy: Theoretical Concepts, Measurements and Applications*; Elsevier: Amsterdam, 2001, p 167.

(73)   Gilroy, K. D.; Ruditskiy, A.; Peng, H. C.; Qin, D.; Xia, Y. Bimetallic nanocrystals: Syntheses, properties, and applications. *Chemical Reviews* **2016**, *116*, 10414–10472.

(74)   Decarolis, D.; Lezcano-Gonzalez, I.; Gianolio, D.; Beale, A. M. Effect of Particle Size and Support Type on Pd Catalysts for 1,3-Butadiene Hydrogenation. *Topics in Catalysis* **2018**, *61*, 162–174.

(75)   Silvestre-Albero, J.; Rupprechter, G.; Freund, H. J. Atmospheric pressure studies of selective 1,3-butadiene hydrogenation on Pd single crystals: Effect of CO addition. *Journal of Catalysis* **2005**, *235*, 52–59.

(76)   Silvestre-Albero, J.; Rupprechter, G.; Freund, H. J. Atmospheric pressure studies of selective 1,3-butadiene hydrogenation on well-defined Pd/Al2O3/NiAl(110) model catalysts: Effect of Pd particle size. *Journal of Catalysis* **2006**, *240*, 58–65.

(77)   Yang, X. F.; Wang, A. Q.; Wang, Y. L.; Zhang, T.; Li, J. Unusual Selectivity of Gold Catalysts for Hydrogenation of 1, 3-Butadiene toward cis-2-Butene: A joint experimental and theoretical investigation. *Journal of Physical Chemistry C* **2010**, *114*, 3131–3139.

(78)   Delannoy, L.; Thrimurthulu, G.; Reddy, P. S.; Méthivier, C.; Nelayah, J.; Reddy, B. M.; Ricolleau, C.; Louis, C. Selective hydrogenation of butadiene over TiO 2 supported copper, gold and gold–copper catalysts prepared by deposition–precipitation. *Phys. Chem. Chem. Phys.* **2014**, *16*, 26514–26527.